

Intrinsically DRC-Compliant Nanophotonic Design via Learned Generative Manifolds

Bahrem Serhat Danis,¹ Demet Baldan Desdemir,¹ Enes Akcakoca,¹ Zeynep Ipek Yanmaz,¹ Gulzade Polat,¹ Ahmet Onur Dasdemir,¹ Aytug Aydogan,² Abdullah Magden,³ and Emir Salih Magden^{1,4,*}

¹Dept. of Electrical and Electronics Engineering, Koç University, Istanbul, 34450, Turkey

²KU Leuven, Dept. of Physics and Astronomy, B-3000 Leuven, Belgium

³Dept. of Mathematics, Faculty of Engineering and Natural Sciences, Bursa Technical University, Bursa, 16310, Turkey

⁴KUIS AI, Koç University, Istanbul, 34450, Turkey

Inverse design has enabled the systematic design of ultra-compact and high-performance nanophotonic components. Yet enforcing foundry design rules during inverse design remains a major challenge, as optimized devices frequently violate constraints on minimum feature size and spacing. Existing fabrication-constrained approaches typically rely on penalty terms, projection filters, or heuristic binarization schedules, which restrict the accessible design space, require extensive hyperparameter tuning, and often fail to guarantee compliance throughout the optimization trajectory. Here, we introduce a framework for nanophotonic inverse design with intrinsic enforcement of design rules through a generative reparameterization of the design space, restricting optimization to a learned manifold of DRC-compliant geometries. We validate this paradigm by designing representative silicon photonic components including broadband power splitters, spectral duplexers, and mode converters operating across the 1,500–1,600 nm band for both electron-beam lithography and photolithography platforms. Across all devices, the manifold-based formulation reaches state-of-the-art performance metrics with over a 5-fold reduction in computational cost compared to pixel-based representations, while ensuring fabrication-compatible geometries throughout the entire design process. By treating fabrication constraints as a fundamental property of the design representation rather than an external penalty, this work establishes a direct pathway toward broadly applicable, platform-agnostic, and intrinsically DRC-compliant nanophotonics.

I. INTRODUCTION

Integrated photonic components are indispensable for high-speed communications [1, 2], sensing [3], and computation [4, 5], as they combine low propagation losses with wide bandwidths [6–11] in compact footprints [12–17]. Achieving such performance, however, requires design methodologies that go beyond fundamental understanding of light propagation [18], mode coupling dynamics [19], or typical designer intuition [20]. In this domain, inverse design has emerged as a powerful paradigm for realizing photonic devices with superior performance, as many of these geometries are prohibitively complex to create manually [21–25]. By leveraging algorithmic design procedures, many different classes of devices, including wavelength-dependent and polarization-sensitive optical signal processors [26, 27], high-speed modulators [28, 29], and compact multimode grating couplers [30], have already been demonstrated. In these design approaches, a target device response is first specified, and an algorithm iteratively refines a set of geometrical parameters to improve a quantitative figure of merit through gradient-based optimization. The material topology or shape distribution within the design region is optimized by iteratively updating parameters according to these gradients, ultimately converging toward geometries that achieve the desired performance objectives [31–33]. Even though inverse design of photonic

structures has produced impressive results, the underlying optimization problem is inherently ill-posed [34]. For a given target optical operation, there typically exists not a single unique geometry but a vast family of structures that all yield acceptable results in terms of extinction ratio, insertion loss, or related performance metrics. Moreover, designers typically seek a solution that performs acceptably well rather than the absolute global optimum, further broadening the solution space [35–37]. This reflects a broad, high-dimensional set of geometries that effectively yield indistinguishable optical responses, or perform equally well within a given application space.

On the other hand, practical use and scalability are only possible for a small subset of these geometries that are also fabrication compliant. Layouts of fabrication-compatible devices must satisfy design rules such as minimum feature size, curvature limits, enclosed-area requirements, and angle-of-curvature conditions. If these rules are not enforced during the design stage, the resulting geometries risk being fabrication-incompatible, leading to partial pattern transfer, degraded performance, or complete device failure [38, 39]. One major strategy to enforce fabrication compatibility in inverse-designed structures begins with a grayscale representation and applies averaging and projection operations to gradually guide the optimization toward smooth, discrete geometries with well-defined material boundaries. To avoid disrupting convergence, many implementations carefully schedule the averaging resolution and projection strength, since applying strong discretization or large spatial filters too early can cause the optimization to stagnate or yield suboptimal devices. This process often requires hundreds

* Corresponding author: esmagden@ku.edu.tr

of iterations, as progressively stronger discretization and larger feature sizes inherently increase the difficulty of convergence. Moreover, the outcome can be sensitive to hyperparameter choices, frequently necessitating restarts or fine-tuning of the optimization schedule, which limits efficiency and scalability [40–44]. Other strategies construct devices entirely from smaller, rule-compliant building blocks [25, 45, 46] or phase-projection-based generators [47]. While this guarantees fabrication compatibility by design, the restricted design space often forces a trade-off, sacrificing either high performance or overall footprint compactness for the desired operation.

The combination of a vast solution space and the stringent fabrication compatibility requirements motivates a fundamentally different design paradigm. In this paper, we introduce a framework for nanophotonic inverse design that utilizes a generative reparameterization to directly parameterize fabrication-compatible devices as a low-dimensional manifold of design rule check (DRC)-compliant geometries within the much larger set of possible solutions. By reparameterizing the design search, the ill-posed optimization problem is transformed into a tractable, intrinsically fabrication-compliant framework. Our generator network is trained with fabrication-compatibility metrics that enforce minimum feature size and discrete topology while ensuring compatibility with standard CMOS design rules. We demonstrate this framework across a variety of devices including power splitters, wavelength multiplexers/demultiplexers, as well as mode converters, and show that optimization converges in significantly fewer iterations while maintaining fabrication compliance throughout. Furthermore, by simply adjusting the spatial resolution of the generator layers, we demonstrate that the same approach can be applied to different fabrication platforms, from electron-beam lithography (EBL, 60 nm minimum feature size) to photolithography (PL, 150 nm minimum feature size). This integration yields high-performance, fabrication-compatible devices while significantly reducing optimization time, offering a scalable pathway toward the next generation of design-rule-compliant integrated photonic technologies.

II. MANIFOLD REPARAMETERIZATION FOR INTRINSICALLY FABRICATION-COMPLIANT INVERSE DESIGN

In conventional pixel-based inverse design, achieving a high-performance device involves continuously updating the design parameters that describe the permittivity distribution of the core and cladding regions. In practice, the design region is discretized into a grid of pixels, and the value of each pixel's permittivity is iteratively adjusted during device search until a distribution yielding desirable device performance is obtained. Each vector x representing a pixel-based permittivity distribution in the search space. The set of all possible vectors therefore

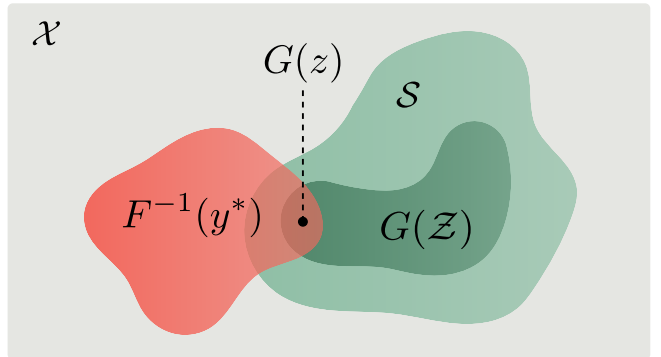


FIG. 1. Conceptual illustration of search domains and solution sets in inverse design. The ambient design space is denoted by \mathcal{X} . The set $F^{-1}(y^*)$ corresponds to all permittivity distributions that achieve the desired target response y^* . The subset $\mathcal{S} \subset \mathcal{X}$ represents the space of fabrication-compatible permittivity distributions. DRC-compliant solutions therefore lie in the intersection of $F^{-1}(y^*) \cap \mathcal{S}$. The generative manifold $G(\mathcal{Z})$, parameterized by the latent space \mathcal{Z} , is embedded within the subset \mathcal{S} , ensuring fabrication compatibility by construction. $G(z)$ denotes one feasible solution within the manifold.

forms the design space \mathcal{X} , as illustrated in Fig. 1. Since conventional inverse design explores the permittivity distribution explicitly via a direct search over pixel-based solutions, this space \mathcal{X} functions as an ambient search domain. During device optimization, the proximity of the current device response to the target response is evaluated through electromagnetic solvers. These solvers take the permittivity distribution as input and produce the corresponding device response, formally described by a response function $F(x)$. The goal is to identify a permittivity distribution that yields the desired target response y^* . The device search systematically explores candidate distributions $x \in \mathcal{X}$ to find an appropriate solution that satisfies $F(x) = y^*$. However, since different permittivity distributions can produce similar or even identical responses, this inverse problem is inherently ill-posed as many non-unique solutions exist for a given y^* . The set of all these solutions is a subspace of \mathcal{X} denoted by $F^{-1}(y^*)$ in Fig. 1. In addition to finding appropriate solutions, the optimization process also incorporates a regularization term $R(x)$ governing the transformations applied to the permittivity distribution such as the scheduling of spatial averaging, filtering, and projection operations. Physically, $R(x)$ enforces design-rule compliance including minimum feature size, minimum enclosed area, and curvature constraints, while guiding the distribution toward a well-defined material boundary form suitable for fabrication. This forces the optimization to converge to a solution within \mathcal{S} , the set of all fabrication-compatible devices where $\mathcal{S} \subset \mathcal{X}$. Mathematically, this inverse problem can thus be expressed as

$$\arg \min_{x \in \mathcal{X}} \left\{ \|F(x) - y^*\|^2 + R(x) \right\}. \quad (1)$$

Because the inverse mapping $F^{-1}(y^*)$ is inherently ill-posed, these regularizers are indispensable. However, by imposing constraints on the inverse problem, they further complicate convergence of optimization, often necessitating a large number of iterations. Moreover, since the regularization term can be applied in distinct forms at each iteration according to a predetermined schedule, it introduces pronounced sensitivity to hyperparameter selection, and limits the overall scalability and robustness of the approach.

Instead of conducting the search directly in the ambient design space \mathcal{X} , we introduce a fundamentally different methodology in which the inverse design problem is reparameterized on a low-dimensional manifold $G(\mathcal{Z})$, where each $G(z) \in G(\mathcal{Z})$ represents a single fabrication-compatible device geometry in the latent space \mathcal{Z} . Consequently, all solutions in this low-dimensional manifold $G(\mathcal{Z})$ also exist in \mathcal{S} , effectively ensuring that $G(\mathcal{Z}) \subset \mathcal{S}$. Within $G(\mathcal{Z})$, as optimization is mapped onto a lower-dimensional parameter space, convergence toward appropriate solutions is achieved much faster. In addition, as DRC-compliance is intrinsically enforced by the structure of the manifold $G(\mathcal{Z})$, conventional regularization strategies such as minimum feature size rules, curvature constraints, or material boundary penalties are no longer required for fabrication compatibility. Therefore, the optimization search reduces to a direct comparison between the device response and the target response expressed as

$$\arg \min_{z \in \mathcal{Z}} \left\{ \|F(G(z)) - y^*\|^2 \right\}. \quad (2)$$

As depicted in Fig. 1, the intersection $F^{-1}(y^*) \cap \mathcal{S}$ corresponds precisely to fabrication-compatible solutions that also satisfy the target response. The feasibility of this optimization in such a lower-dimensional latent space relies on the existence of a well-behaved manifold that ensures fabrication compatibility of any $G(z)$ for a given fabrication platform. In the following section, we discuss how this manifold is constructed through a differentiable convolutional deep neural network architecture.

III. INTRINSICALLY DRC-COMPLIANT GENERATIVE MANIFOLD

The goal of the generative manifold is to learn how to map a latent input z to a fabrication-compliant permittivity distribution $G(z)$ that is free of DRC errors, and with smooth/well-defined material boundaries. This is achieved by the sequence of operations depicted by the model in Fig. 2(a). This model takes as input a low-dimensional, grayscale array with values in the $[0, 1]$ range, and processes it through four cascaded upsampling

operations, each one enlarging its input by a factor of 1.4. This cascaded upsampling allows for multiple smaller steps to effectively construct a larger composite interpolation filter, allowing for a larger part of the final device to be influenced by a broader set of original input values, and mitigating excessive smoothing typically introduced by a single, large interpolation kernel. The model then applies three successive upsampling-convolution operations with 32, 16, and 1 kernels of size 5×5 , respectively. This approach is more appropriate for creating smooth geometries, as it prevents the emergence of checkerboard artifacts resulting from more typical transposed convolution operations. Each convolution is followed by a softmax activation. Following these three stages are an additional sequence of upsampling, modified softmax, and morphological closing operations. This modified softmax operation is configured with a scheduled slope parameter allowing for it to be updated during training, and is used for gradually guiding the formation of well-defined material boundaries during training. The closing operation performs morphological smoothing that fills small gaps and connects narrow openings over a 3×3 window to generate the final device geometry. This specific construction of the generator allows for a size-agnostic input-output mapping as all upsampling, convolution, softmax nonlinearity, and morphological closing blocks operate independent of the input dimensions. This means that the model can generate layouts of varying dimensions simply by adjusting the input size. As such, the optimization within the latent space can be performed for any desired target device footprint, simply by selecting the corresponding input dimensions.

For efficient and robust training of this generator model, we use a gradient-based approach using forward and backward passes depicted by solid and dashed arrows through each one of the constituent mathematical blocks in Fig. 2(a). Operations including convolution, softmax, and most morphological transformations are routinely implemented in a differentiable manner, providing direct access to the derivative information through the backward pass. However, as the final softmax layer with the scheduled slope acts as a non-differentiable thresholding operation by the end of training, this layer requires special consideration for its derivative. To mitigate this, we use a straight-through estimator (STE) [48] to handle this non-differentiable block for the computation of a slightly inaccurate, yet still sufficient estimate of the gradient.

Using this gradient information, we train the generator with a topological loss function that incorporates geometric constraints such as minimum width and spacing. Furthermore, since sharp corners also constitute a design rule violation, the loss implicitly includes a curvature constraint to ensure all generated edges are smooth and fabrication-compatible relative to the specified minimum feature size. The upsampling layers in the generator further reinforce this curvature constraint by expanding small feature maps into larger ones while also

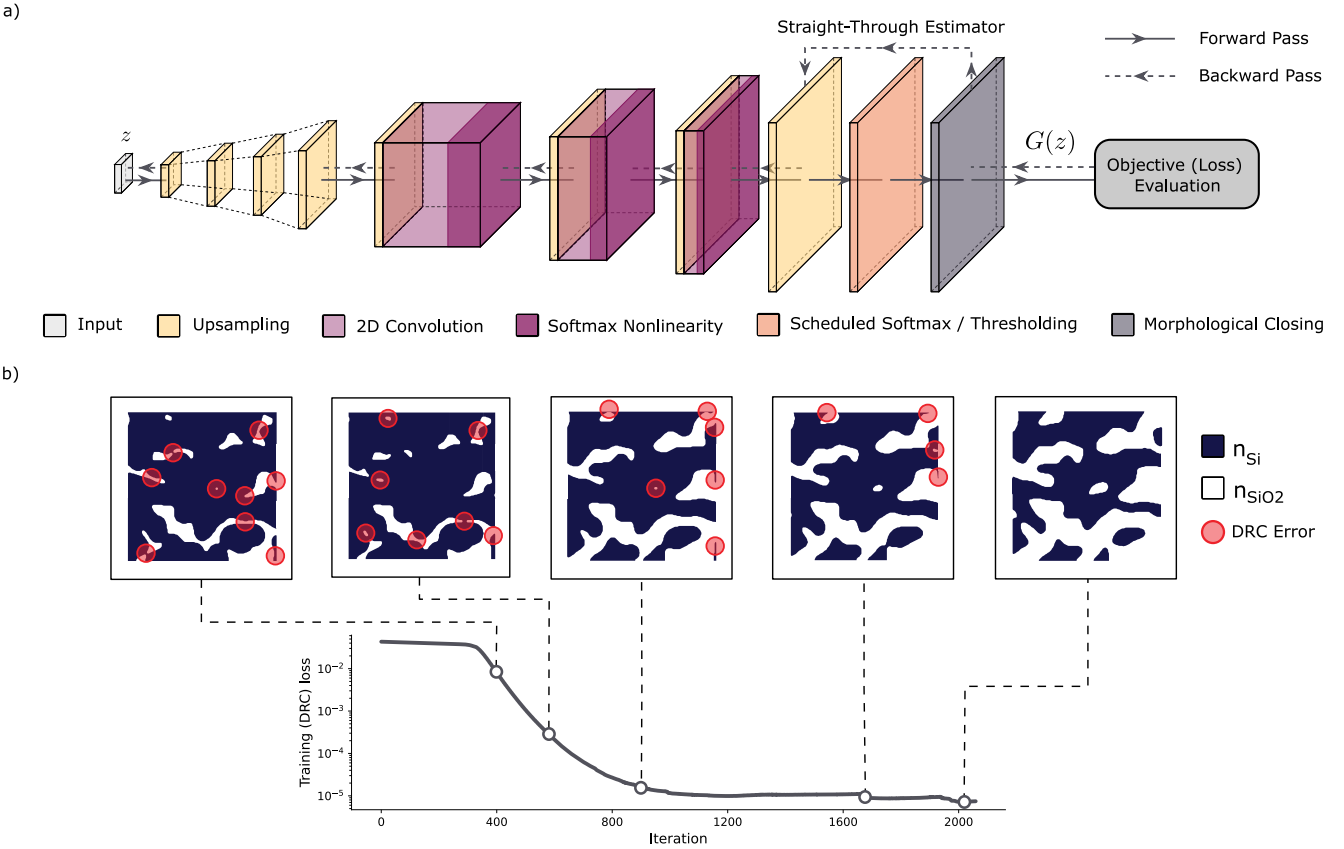


FIG. 2. DRC-compliant generative model for electron-beam lithography. (a) Schematic of the proposed architecture, illustrating the sequence of operations from a latent variable z to the final device layout. The generator comprises four cascaded upsampling stages followed by three upsampling-convolutional layers, with nonlinear transformations including softmax, thresholding, and morphological closing to ensure design-rule compliance. The straight-through estimator (STE) is employed in the backward pass to preserve gradient flow despite the non-differentiable thresholding step. The generated structure $G(z)$ is evaluated through a design objective (DRC loss) and is iteratively optimized. (b) Training dynamics of the model. The DRC loss decreases from 3×10^{-2} to 7×10^{-6} , representing a reduction by over four orders of magnitude. Insets show representative permittivity distributions at different training stages, with silicon (n_{Si}), silica (n_{SiO_2}), and DRC errors (red circles) highlighted. As training progresses, violations are systematically eliminated, and the final distribution satisfies DRC constraints with no residual errors.

performing spatial smoothing. Using a single-etch silicon photonic platform with boundaries between Si and SiO_2 materials, we formulate this topological loss [40] as

$$\begin{aligned} \mathcal{L} = & \sum_{i,j} I_{i,j}^{LW}(\rho) \cdot [\min\{(\rho_{i,j} - \eta_e), 0\}]^2 \\ & + I_{i,j}^{LS}(\rho) \cdot [\min\{(\eta_d - \rho_{i,j}), 0\}]^2. \end{aligned} \quad (3)$$

Here, ρ represents a normalized permittivity distribution between 0 (SiO_2) and 1 (Si), while the scalars η_d and η_e serve as permittivity thresholds (between 0 and 1) for the erosion and dilation operations. The auxiliary functions I_{LW} and I_{LS} represent inflection regions that determine whether the design topology remains invariant under a strategically chosen sequence of erosions and dilations, see Supporting Information 1. As constructed, this loss function does not explicitly include terms for minimum area or minimum enclosed area. Instead, the generator

automatically removes small islands through the differentiable morphological closing layer, whose kernel size exceeds the minimum feature size. Likewise, smoothing introduced by the initial cascaded upsampling prevents the formation of small holes, thereby ensuring compliance with the minimum enclosed area requirement.

For characterizing the performance of a device created with this process, the input and output waveguides are placed before the morphological closing operation. This sequence ensures fabrication-compatible connections between the device geometry and the attached waveguides. For this specific generator and loss function, we specify minimum width and spacing as 60 nm, for compatibility with standard EBL processes available. The model also allows for configuration with larger feature sizes for PL, as discussed in the later sections.

To train this generator, we created a custom dataset of inputs by representing 2D noisy latent space distributions

using Perlin noise, as it produces smooth yet stochastic variations across multiple length scales [49]. Compared to pixel-based uncorrelated random noise, this approach yields a highly diversified training distribution by capturing both pixelated, spatially high frequency patterns as well as inputs with large geometrical features. To incorporate diversity throughout the dataset, we generated 1000 unique samples by randomly varying the scale, offset, and noise dimensionality, thereby obtaining multiple granularities across different topologies for improving the generalization capabilities of the generator. These parameters control the relative sizes of textures, spatial shifts and alignment of features, and number of independent stochastic components that define each pattern. For more details on each one of these parameters, and visual comparison of the latent space samples, see Supporting Information 2. We constrained each input distribution to lateral dimensions between 4 and 45 pixels in each direction, such that the dataset covers multiple physical device sizes between $1\text{ }\mu\text{m}$ and $20\text{ }\mu\text{m}$, after the generator upscaling. The input/output mapping between pixels in the latent space and physical dimensions in the device space are provided in Supporting Information 3.

The generator was trained using an ADAM optimizer as shown in Fig. 2(b). The goal of this training procedure is to effectively shape $G(\mathcal{Z})$ according to the loss function specified above, such that the output devices are all intrinsically fabrication-compliant. The generator model begins with a DRC loss of 4×10^{-2} , decreases slowly over the first 300 iterations, and falls further as the generator outputs sharpen, ultimately reaching 8×10^{-6} after 2060 iterations (see Methods for more training details). With this progression, the number of DRC violations for generated devices also gradually decreases. This is illustrated by snapshots of the output $G(z_0)$ provided throughout the training, for a specific input z_0 . The training procedure gradually modifies the generator parameters to smooth and correct regions violating minimum length and spacing constraints, eliminating DRC errors in the process. At the end of training, the manifold $G(\mathcal{Z})$ is effectively a subset of \mathcal{S} (the set of all fabrication-compliant devices), ultimately producing an intrinsically DRC-compliant model where all inputs in the latent space correspond to physically DRC-clean device layouts.

During the inference of the trained generator, the scheduled softmax is replaced with a thresholding operation to obtain a discrete layout. Since this thresholding layer is non-differentiable, its gradient is approximated using the STE introduced earlier, allowing the entire generator and pipeline to remain differentiable and enabling gradient-based optimization of the latent space.

IV. DEVICE OPTIMIZATIONS

In this section, we demonstrate the versatility of our generator by designing several representative classes

of photonic devices including power splitters, spectral mux/demux, and a mode converter. The device optimization pipeline is constructed through modular computational blocks. For all devices, the generator first creates the device's geometry $G(z)$ from the latent space representation z . This is followed by a differentiable electromagnetic simulator and the final objective (loss) evaluation based on the specified target functionality. An optimizer then iteratively updates the latent space representation z according to this objective evaluation. This modular construction allows users to utilize any differentiable electromagnetic simulator that suits their application [33, 50–52]. For our specific applications, we employ a factorization-cached implementation of the Finite-Difference Frequency-Domain (FDFD) solver, which stores and reuses the matrix factorizations of the discretized Maxwell's equations throughout the iterative design process [53]. The optimizations are carried out over a broadband wavelength range from 1500 nm to 1600 nm using a single-etch, 220-nm-tall Silicon-on-Insulator (SOI) platform. For the power splitters and spectral mux/demux devices, we use the fundamental transverse electric modes (TE_0) of 450-nm-wide input and output waveguides. The mode converter features a larger output waveguide width (750 nm) to support a guided TE_1 mode. This entire pipeline is designed to confine the device optimization procedure to a low-dimensional, fabrication-aware subspace. As a result, the generated final devices are guaranteed to both satisfy the objective photonic functionality as closely as possible and be free of any DRC errors.

Design of Broadband Power Splitters with Variable Splitting Ratios

To place our proposed approach within the existing inverse design domain, we first compare it against conventional, pixel-based inverse design methods by designing a compact, broadband 50/50 power splitter as a benchmark device. The dimensions of this benchmark device are identical at $4.2 \times 4.2\text{ }\mu\text{m}^2$ for both our proposed method and the conventional approach. The target condition is that the optical power is evenly distributed between the two output waveguides within the 1500–1600 nm wavelength range. In conventional inverse design, the device geometry is represented by individual grayscale pixels, which are iteratively updated during optimization. Operations such as averaging and projection operations are applied over the pixel field to drive pixel values towards 0 or 1 for enforcing discretization and creating distinct material boundaries. These operations are typically updated through pre-determined or adaptive schedules, effectively redefining the optimization problem with each iteration [21, 23, 32, 40]. The scheduled update of the discretization projection strength often introduces abrupt changes in the objective function, and requires further optimization for the device performance to be recov-

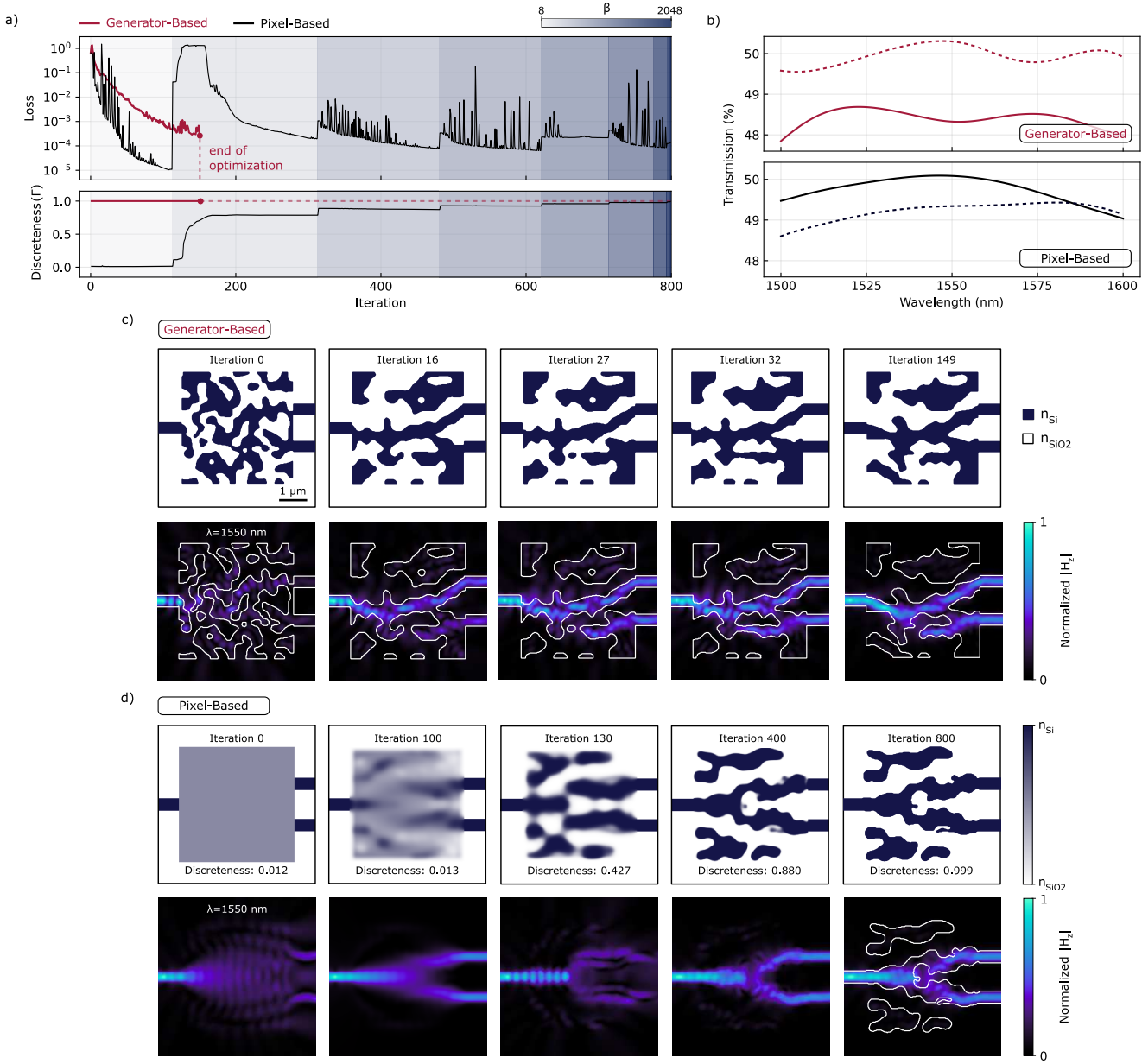


FIG. 3. Comparison of generator-based and pixel-based inverse design for 50/50 power splitters. (a) Evolution of the loss function and Γ during optimization. The generator-based method (red) converges to a loss of 2.8×10^{-4} within 149 iterations while maintaining full discreteness of 1 throughout. In contrast, the pixel-based method (black) reaches a lower loss of 1.3×10^{-4} after 800 iterations, but requires progressive increases in the projection strength parameter β (color-coded, from 8 to 2048) to approach discretization, corresponding to over a 5-fold reduction in computational cost with the generator-based formulation. (b) Transmission spectra of the optimized devices, where solid and dashed lines denote the bottom and top output ports, respectively. (c) Generator-based optimization: snapshots of the permittivity distribution (top) and the corresponding normalized magnetic field $|H_z|$ at $\lambda = 1550$ nm (bottom) across representative iterations. The white contours denote the silicon boundaries. The design remains strictly discrete at every iteration. (d) Pixel-based optimization: analogous snapshots of permittivity (top) and $|H_z|$ fields (bottom), illustrating gradual discretization that is only fully achieved at the final iteration. Γ in each snapshot quantitatively tracks this transition.

ered [40, 41, 43]. This behavior is illustrated by the black curves in Fig. 3(a), where successive increases in the objective correspond to scheduled increments of the discretization strength parameter (β). This parameter

controls the slope of a sigmoid function used to drive individual pixels towards SiO_2 (0) or Si (1) (see Methods). Introducing strong discretization too early in the optimization can lead to difficult convergence, entrap-

ment in local minima with insufficient performance, and a significantly slower overall process [43, 54, 55]. Although gradual discretization circumvents these issues, it also requires a substantial number of iterations to explore grayscale, unrealizable geometries with ill-defined material boundaries, thereby limiting both optimization efficiency and practical utility. For this device, convergence is achieved with a final objective of 1.3×10^{-4} in 800 iterations (see Methods for convergence conditions), after which the objective does not significantly improve. The discreteness metric Γ , (defined as the portion of black & white pixels, see Supporting Information 4) begins at 0.01, corresponding to a nearly fully grayscale device, and increases proportionally with projection-strength updates until it approaches 1, representing well-defined material boundaries.

In contrast, the generator-based approach inherently constrains the search to fabrication-compliant geometries, allowing for a much more efficient exploration of the design space while inherently satisfying design rule constraints. This approach avoids the abrupt changes in the objective function, and maintains well-defined material boundaries throughout the entire optimization as shown by the red curves in Fig. 3(a). For a device with identical dimensions, convergence is reached in 149 iterations, over 5-times faster than the conventional method, with a final objective of 2.8×10^{-4} . Unlike the gradually discretized device in traditional inverse design, the gradient-based approach maintains a fully discretized geometry throughout the entire optimization process, as indicated by the constant Γ at 1.

In our generator-based approach, the underlying optimization framework remains structurally identical to conventional inverse design, with the exception of inference through the trained generator. These added steps only marginally increase the per-iteration computational requirements for two key reasons. Firstly, modern Graphics Processing Units (GPUs) are highly optimized for parallel processing of image-based operations, including the convolutions and point-based nonlinearities used in the generator architecture. This inherent parallelism ensures the generator inference remains computationally efficient. More importantly, in both conventional and generator-based methods, the physical device simulations consume the vast majority of the computational resources for each iteration [20, 33, 47]. As a result, our generator-based design process offers a highly favorable trade-off resulting in a significantly reduced iteration count with marginal additional computational overhead. Crucially, the generator-based optimization process requires no regularization or objective scheduling to enforce material boundaries. This elimination of scheduled parameter updates also streamlines the design process, making it significantly more robust and usable for designers, with no need for repeated parameter tuning, optimization restarts, or manual intervention. These differences highlight the generator-based methodology as a more efficient, autonomous, and parameter-independent

inverse design platform compared to conventional methods.

Fig. 3(b) illustrates the transmission spectra for both optimized devices, with dashed and solid lines representing the top and bottom output ports, respectively. Both approaches yield devices with good performance, maintaining a near-ideal 50/50 power-splitting ratio across the entire 1500–1600 nm wavelength range. Fig. 3(c) and Fig. 3(d) present the final device geometries and the normalized H_z field profiles at 1550 nm, as obtained through Finite-Difference Frequency-Domain (FDFD) simulations performed on the two devices. DRC procedures confirm that both final geometries fully satisfy the fabrication constraints in addition to their broadband, efficient power splitting functionality. Crucially, the generator-based device maintains its well-defined material boundaries throughout all optimization iterations. This approach eliminates the requirement for gradual increases in discretization strength, which is typically necessary for the convergence of conventional grayscale designs.

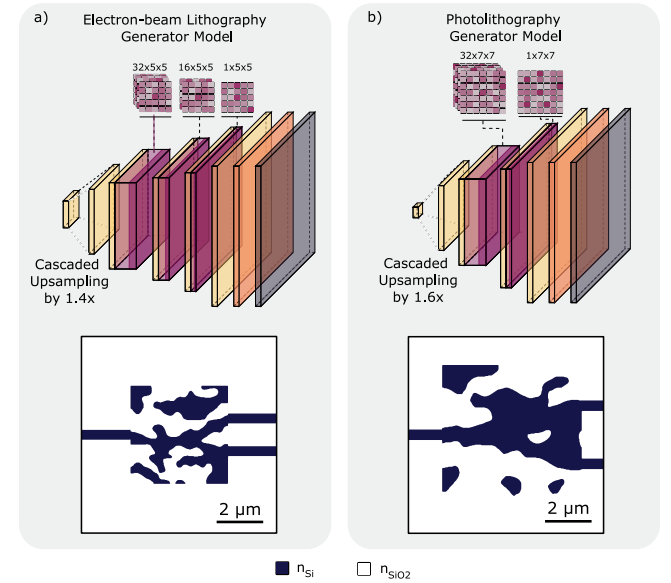


FIG. 4. (a) Architectures of generator models designed for two different lithography models. The electron-beam lithography (EBL) model employs a cascaded upsampling architecture with four $1.4 \times$ upsampling stages. This architecture incorporates three upsampling-convolution layers with varying filter sizes (32, 16, and 1) and a 5×5 kernel. The output is refined using thresholding and morphological closing layers. (b) The photolithography (PL) model features a similar cascaded upsampling architecture, but with four $1.6 \times$ upsampling stages and two upsampling-convolution layers with a 16.1 filter size and a 7×7 kernel. The bottom row of the figure displays the permittivity distributions of a 50/50 power splitter device generated by each model, with footprints of $4.2 \times 4.2 \mu\text{m}^2$ (EBL) and $6 \times 6 \mu\text{m}^2$ (PL). The models are constrained by minimum feature sizes of 60 nm for EBL and 150 nm for PL. The dark blue and white regions represent silicon (n_{Si}) and silicon dioxide (n_{SiO_2}), respectively.

Our generator-based approach provides a general platform for optimization for compatibility with multiple different fabrication methods and foundry standards. We illustrate this by training two separate generators, corresponding to two widely used fabrication technologies: EBL (with 60 nm min. feature size) and PL (with 150 nm min. feature size) as shown in Fig. 4. The larger feature size necessary for the PL generator model was achieved through a greater scaling ratio of 1.6 for each initial upsampling stage, one fewer upsampling-convolution block compared to the e-beam model, and larger convolution kernels of 7×7 in size. Achieving DRC compliance at larger feature sizes requires larger convolutional kernels, effectively expanding the receptive fields of the convolutional layers. To manage the increased precision required for minimum-width and enclosed-area rules at this lower feature size, the 60-nm model utilizes three upsampling convolution layers compared to only two in the 150-nm version. The training of the PL generator model is detailed in Supporting Information 5. The output grid for both the e-beam and photolithography generators were set to a pixel size of $25 \text{ nm} \times 25 \text{ nm}$.

The two 50/50 splitters designed respectively with the two models intrinsically compliant with e-beam and photolithography are shown in the bottom half of Fig. 4. The first device shown here is the same as the one in Fig. 3, and is displayed here for comparison. The second device is the output of the photolithography-compliant generator described above. When using this PL model, we expand the device footprint from $4.2 \times 4.2 \mu\text{m}^2$ to $6 \times 6 \mu\text{m}^2$. This larger design region is necessary because the PL model, constrained by a larger minimum feature size compared to the e-beam model, is less capable of supporting the same design performance within the smaller footprint. This optimization for this device converges after 150 iterations, yielding a final loss value of 2×10^{-3} . The higher loss compared to the e-beam generator model arises from the stricter, larger fabrication constraint of 150 nm. This model is more constrained, and is therefore unable to introduce finer structural details. This reduces the design flexibility, and makes the design task a more challenging problem. Consequently, the lowest attainable local minimum stabilizes around a slightly higher loss, compared to 3.2×10^{-4} obtained with the e-beam-compliant generator. The number of iterations required for convergence remains similar between the two cases since both optimizations operate within comparable latent space dimensions. The transmission spectra, details of the device geometries, and FDFD field plots of the photolithography-compliant power splitter are provided in Supporting Information 6.

To demonstrate the utility and generalization capabilities of our generator models, we design power splitters with arbitrary splitting ratios. Specifically, we demonstrate two additional power splitters with splitting ratios of 30/70 and 10/90. Both devices share the same footprint as the initial 50/50 power splitter, namely $4.2 \times 4.2 \mu\text{m}^2$. For the 30/70 power splitter, we select

six uniformly-spaced wavelengths between 1500 nm and 1600 nm and set target operation at all wavelengths for a top port transmission of 30% and a bottom port transmission of 70%. As shown in Fig. 5(a), the optimization reduces the loss to 5×10^{-4} after 150 iterations. Fig. 5(b) shows that the transmission varies between 27% and 29% at the top port, while it remains between 67% and 69% at the bottom port. The simulated insertion loss of this device is 0.11 dB at 1550 nm. For the 10/90 power splitter, we again select the same six wavelengths, targeting 10% transmission at the top port and 90% at the bottom port. After 150 iterations, the optimization converges to a minimum loss of 4×10^{-4} , as illustrated in Fig. 5(c). Fig. 5(d) shows that the top port transmission between 8% and 10%, while the bottom port transmission varies between 87% and 89%. The simulated insertion loss of this splitter is approximately 0.09 dB. In both optimizations, the local minimum emerges after 150 iterations, similar to the 50/50 power splitter. This consistency can be attributed to the identical latent space dimensions across the three cases. Fig. 5(e) presents the final geometry of the optimized 30/70 splitter, along with the normalized magnetic field magnitude from finite-difference frequency-domain (FDFD) simulations at three different wavelengths, illustrating how the input power distributes across the output ports. Similarly, Fig. 5(f) shows the geometry of the optimized 10/90 splitter and its normalized magnetic field magnitudes at three wavelengths, confirming the designed splitting behavior. These simulated field distributions verify the transmission behavior and the broad operation bandwidth of the optimized devices.

Multi-Wavelength Photonic Duplexer

To further demonstrate the capability of our proposed model, we design a broadband silicon photonic wavelength duplexer as an additional benchmark device. This device routes input light within the 1500–1550 nm wavelength range to the top port, while signals in the 1550–1600 nm wavelength range are directed to the bottom port, effectively realizing short-pass and long-pass output ports. The footprint of the device is $7 \times 7 \mu\text{m}^2$, with a corresponding latent space dimension of 28×28 . For the optimization objective, we use ten target wavelengths between 1500 nm and 1600 nm. The first five wavelengths are set to achieve 100% transmission into the top port, while the remaining five wavelengths are targeted for 100% transmission into the bottom port.

After 160 optimization iterations, a minimum loss of 1×10^{-2} is achieved, as shown in Fig. 6(a). The abrupt jump in the loss function observed around iteration 70 is a direct consequence of the optimizer's trajectory as it navigates the complex loss landscape of the latent space. This discontinuity suggests that the optimizer becomes temporarily trapped in a local minimum, and subsequently transitions to a more favorable region of the search space. As illustrated in Fig. 6(b), the device

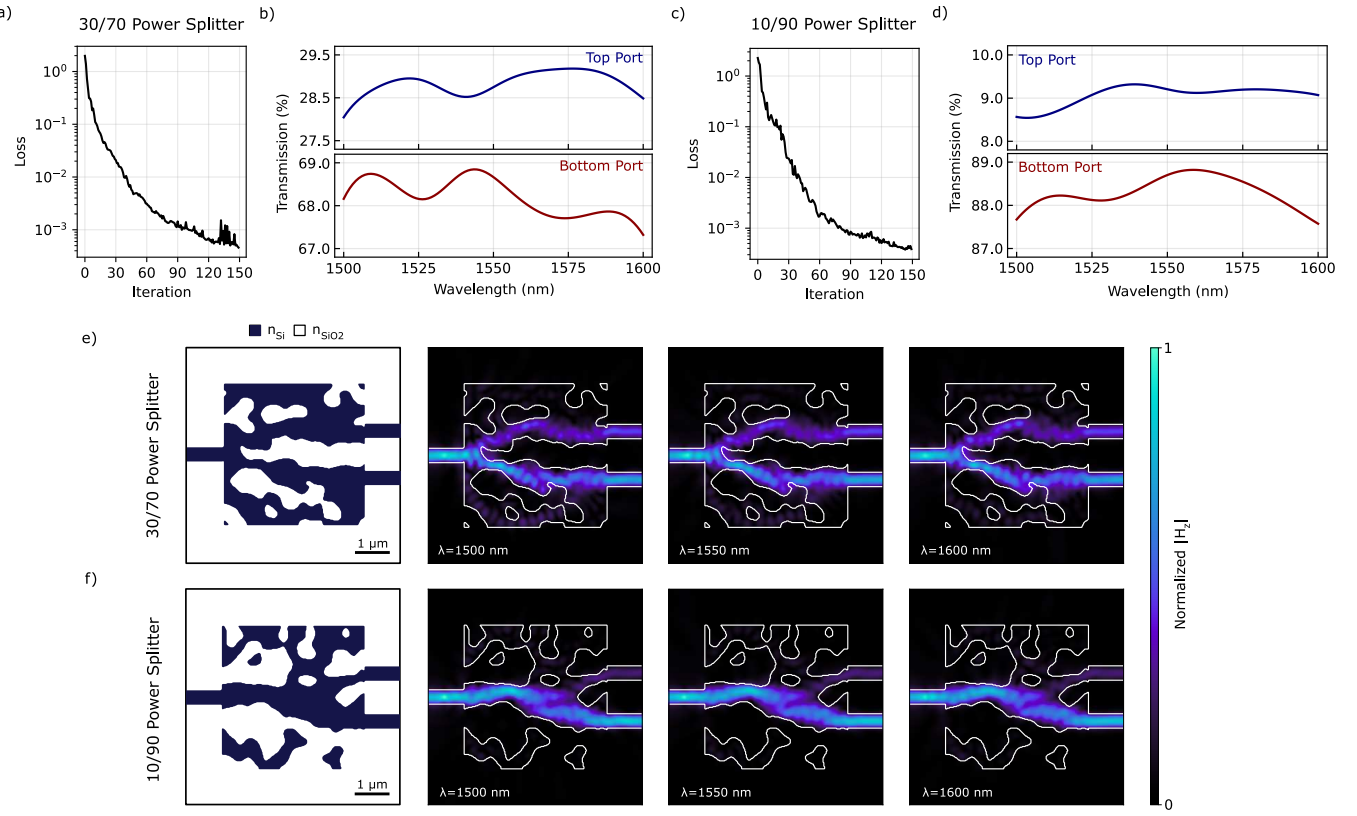


FIG. 5. Ultrabroadband 70/30 and 90/10 power splitter results designed with the electron-beam lithography generator model. (a) Optimization loss curve for the 30/70 power splitter, showing the loss decreasing to 5×10^{-4} over 150 iterations. (b) Transmission curves for the top and bottom ports of the 30/70 power splitter, demonstrating stable performance across the 1500–1600 nm wavelength range. (c) Optimization loss curve for the 10/90 power splitter, converging to a loss of 4×10^{-4} after 150 iterations. (d) Transmission curves for the top and bottom ports of the 10/90 power splitter. (e) Permittivity distribution of the 30/70 power splitter (left, with silicon in dark blue and SiO_2 in white), alongside the normalized magnetic field (H_z) distribution at wavelengths of 1500, 1550, and 1600 nm. The wavelength-insensitive field profiles indicate that the splitting ratio remains constant across the simulated spectrum. (f) Permittivity distribution and normalized magnetic field distribution for the 10/90 power splitter, corresponding to the same wavelengths as in (e).

successfully performs the spectral duplexing operation between the top and bottom ports. The achieved simulated transmission reaches approximately 94%, which corresponds to an insertion loss of only 0.25 dB. The geometry of the obtained wavelength demultiplexer reveals the distribution of SiO_2 and Si materials, with a successful DRC verification. Fig. 6(c) plots the normalized FDFD magnetic field distributions at 1500, 1550, and 1600 nm, which clearly demonstrate how the device routes input signals to the corresponding output ports across different wavelengths.

Broadband Photonic Mode Converter

We also design a broadband mode converter whose purpose is to transform the fundamental TE_0 mode at the input into the TE_1 mode at the output. Since this task is relatively simple compared to other devices, we use a significantly smaller design footprint at $2.1 \times 2.1 \mu\text{m}^2$.

In the optimization, we set the objective to achieve a 100% overlap with the TE_1 electric field distribution at the output port. As shown in Fig. 7(a), the loss reaches a minimum of 3×10^{-4} . In this case, the optimization is carried out in a latent space of dimension 10×10 , which is sufficient for the device to converge to a local minimum within 130 iterations. Fig. 7(b) illustrates that transmission to the TE_1 output remains between 98% and 100%, with a simulated insertion loss of only 0.03 dB at 1550 nm. The device geometry is presented in Fig. 7(c) with additional field plots at wavelengths of 1500, 1550, and 1600 nm verifying broadband and near-lossless operation in a compact footprint.

V. DISCUSSION

The generator model presented in this work achieves state-of-the-art, broadband device performance within compact footprints across a broad spectrum of photonic

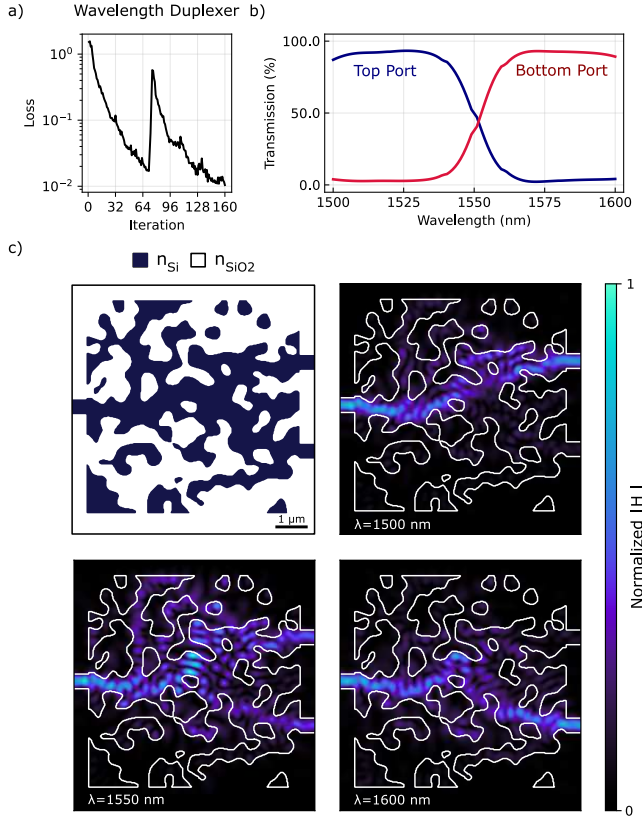


FIG. 6. Photonic duplexer designed with the electron-beam-lithography-compliant generator model. (a) Optimization loss curve of the wavelength demultiplexer, showing a rapid decrease to 1×10^{-2} after 160 iterations. (b) Transmission spectra of the optimized duplexer, demonstrating efficient separation between the top and bottom output ports with peak transmission of 94% (corresponding to an insertion loss of 0.25 dB). (c) Final device layout (top left), where the permittivity distribution is represented with silicon in dark blue and SiO_2 in white. The device satisfies all design rule constraints. The accompanying field maps illustrate the normalized FDFD magnetic field distributions at 1500, 1550, and 1600 nm, confirming robust duplexing functionality across the operating wavelength range.

functionalities. It also demonstrates utility across multiple fabrication platforms including EBL and PL. This approach provides multiple advantages compared to existing DRC-compliance methods in the literature. In contrast to building-block-based methods which ensure compliance by tiling the design region with fixed sub-wavelength primitives [25], our generator avoids reliance on rigid geometric definitions. This flexibility allows the optimization to explore a significantly richer design space. As a result, it achieves superior performance and greater geometric diversity, without relying on discrete building blocks or resulting discretization artifacts. Compared with prior generator-based topology optimization approaches of two-phase projections [47] or brush-based painting [45], our model directly learns a high-

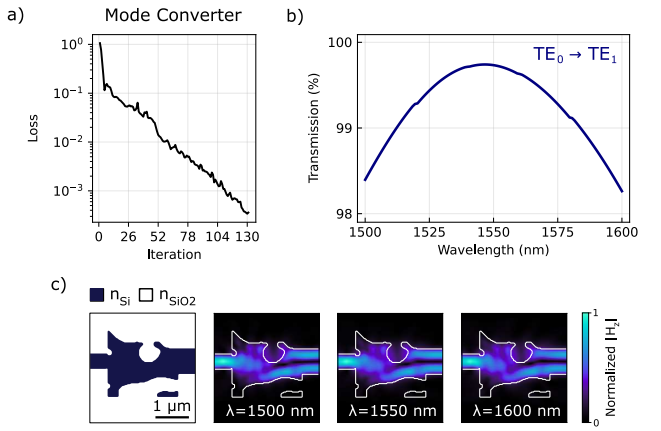


FIG. 7. Results of the broadband photonic mode converter. (a) Convergence of the optimization loss to 3×10^{-4} over 130 iterations. (b) The simulated transmission curve for the mode converter, showing a TE_0 to TE_1 conversion ratio between 98% and 100% across the wavelength range of 1500–1600 nm. The conversion efficiency reaches $\sim 99\%$ at 1550 nm, corresponding to an insertion loss of only 0.03 dB. (c) The optimized device permittivity distribution (left) and the simulated normalized magnetic field distributions ($|H_z|$) at input wavelengths of 1500, 1550, and 1600 nm.

dimensional, fabrication-aware mapping. This architecture supports continuous design updates without violating DRC constraints. Consequently, it improves convergence stability and adapts more readily across disparate fabrication methodologies. Finally, unlike projection-based methods augmented by in-process [43] or post-process regularization [44], our generator does not impose any design constraints retrospectively. By enforcing DRC compliance natively throughout the entire optimization trajectory, we eliminate the need for scheduled or iterative corrective steps that often introduce artifacts, degrade performance, or result in sharp increases in the objective function. The combination of these advantages yields devices that consistently maintain smooth boundaries while respecting minimum feature size constraints across a wide variety of photonic tasks.

A quantitative comparison of simulation results in Table I reveals that our approach consistently establishes a new performance benchmark across all three device categories. While traditional methods like two-phase projection generator (TPPG) and brush-based generator (BBG) typically yield insertion losses between 0.24 dB [47] and 1.17 dB [45], our method achieves a significant breakthrough, particularly in the mode converter, where loss is reduced to a near-negligible 0.03 dB. Even when other designs offer slightly smaller footprints, they often do so at the cost of higher loss or significantly more iterations. For instance, while the structure transformation method requires 450 iterations to reach a 0.46 dB loss for the power splitter, our method settles at a superior 0.12 dB in just 150 iterations. In the

Reference	Power Splitter			Wavelength Duplexer				Mode Converter		
	IL (dB)	Footpr. (μm^2)	Iter.	IL	Footpr.	ER (dB)	Iter.	IL	Footpr.	Iter.
Wang <i>et al.</i> [25]	0.32	2.6×2.6	50	—	—	—	—	—	—	—
Chen H. <i>et al.</i> [47]	0.24	3.0×2.6	75	0.62	3.0×3.0	12	150	0.24	2.6×3.0	100
Schubert <i>et al.</i> [45]	0.34	3.2×2.0	150	1.17	6.4×6.4	20	150	0.45	1.6×1.6	100
Chen Y. <i>et al.</i> [43]	0.46	2.8×2.8	450	—	—	—	—	—	—	—
Hiesener <i>et al.</i> [44]	—	—	—	—	—	—	—	0.64	6.0×3.0	120
Our work	0.12	4.2×4.2	150	0.25	7.0×7.0	16	160	0.03	2.1×2.1	130

TABLE I. Performance comparison of the proposed DRC-compliant inverse design method with previously reported simulation results from approaches for power splitters, wavelength demultiplexers, and mode converters.

case of the wavelength demultiplexer, our design strikes a critical balance by providing a 16 dB extinction ratio, successfully bridging the gap between TPPG’s low loss and BBG’s higher isolation. Furthermore, the mode converter results highlight a dramatic efficiency gain, as we achieve a $2.1 \times 2.1 \mu\text{m}^2$ footprint, nearly matching the smallest reported size while maintaining a loss profile that is an order of magnitude lower than DRC-correction-based methods. These results indicate that our optimization logic explores the design space more effectively, reaching high-performing geometries that others bypass. Consequently, our approach balances these trade-offs more effectively than the state-of-the-art, delivering the lowest insertion loss in every category while maintaining a competitive iteration count and footprint. These comparisons highlight the effectiveness and versatility of our generator across a diverse class of photonic devices.

VI. CONCLUSION

We introduced a deep learning framework for silicon photonic inverse design that embeds fabrication constraints directly into the optimization process, ensuring that the resulting devices are fabrication-compatible. Our approach reformulates length-scale-constrained topology optimization as a scalable unconstrained stochastic gradient problem and provides a generalizable pathway toward practical high-performance silicon photonic components. By mapping a low-dimensional latent space to intrinsically DRC-compliant well-defined material boundaries, our generator removes the need for post-optimization refinement while allowing efficient gradient-based optimization. Across multiple classes of broadband photonic devices including power splitters with arbitrary splitting ratios, wavelength duplexers, and mode converters, our method produces compact, fabrication-compatible devices that converge rapidly and achieve excellent simulated optical performance. In contrast to prior DRC-compatible strategies that rely on building-block assembly, projection-based regularization, or brush-like generative painting, our latent-space-driven framework unifies fabrication com-

patibility enforcement and topology optimization within a single differentiable model. This unified formulation enables a smooth optimization trajectory through the already feasible design space, avoiding any discontinuities or post-processing overheads seen in other DRC-constrained methods. When benchmarked against other state-of-the-art approaches, our framework consistently achieves lower insertion loss, comparable or smaller footprints, and faster convergence across multiple device classes, underscoring its efficiency and scalability. Ultimately, by treating fabrication constraints as a fundamental property of the design representation rather than an external penalty, this work establishes a direct pathway toward broadly applicable, platform-agnostic, and intrinsically DRC-compliant nanophotonics, suggesting a universal route for integrating design rule compliance into deep generative frameworks and paving the way toward truly automated, foundry-ready inverse design pipelines.

VII. METHODS

In both the conventional pixel-based optimization and our proposed generator-based approach, convergence is achieved as the objective successfully meets or drops below the pre-defined target. This convergence condition ensures that the optimization process continues iteratively until the difference between the current device performance and the target goal is eliminated, signaling that the design requirements have been satisfied. For training both the EBL generator model and the PL generator model, we used the ADAM optimizer with a learning rate of 1×10^{-3} , $\beta_1 = 0.9$, and $\beta_2 = 0.999$, using a batch size of 16. The training was performed for 2060 iterations for the electron-beam generator and 1500 iterations for the PL generator, during which the slope of the scheduled softmax layer was gradually increased from 1 to 10^{30} , effectively approximating a step function by the end of training. All training processes were executed on an NVIDIA A100 GPU using the Flax [56] and JAX [57] libraries, with Optax [58] managing the optimization. For the conventional optimization of the 50/50 power splitter, we used the method of moving asymptotes (MMA) optimiza-

tion algorithm from the NLOpt package [59], which proves to be the most effective in the context of pixel-based optimization in our implementation. Automatic DRC verification of the generated and optimized devices was performed using KLayout. Since the electromagnetic solver constituted the dominant computational cost compared with the generator inference, we employed factorization caching via the Intel oneMKL PARDISO library [60] and executed all optimization steps on a 2.4 GHz Intel Xeon Gold processor with eight cores.

ACKNOWLEDGMENTS

This work is supported by the Scientific and Technological Research Council of Turkey (TUBITAK) under grant number 122E214.

DATA AVAILABILITY

The data that support the findings within this manuscript are available from the corresponding author upon reasonable request.

CODE AVAILABILITY

The trained model architectures and corresponding weights for both the EBL and PL design frameworks are publicly available at <https://github.com/Photonic-Architecture-Laboratories/drcgenerator>.

COMPETING INTEREST

The authors declare no competing interests.

REFERENCES

- [1] Shekhar, S. *et al.* Roadmapping the next generation of silicon photonics. *Nature Communications* **15**, 751 (2024). URL <https://doi.org/10.1038/s41467-024-44750-0>.
- [2] Li, Z. *et al.* High density lithium niobate photonic integrated circuits. *Nature Communications* **14**, 4856 (2023). URL <https://doi.org/10.1038/s41467-023-40502-8>.
- [3] Vollmer, F. & Arnold, S. Whispering-gallery-mode biosensing: label-free detection down to single molecules. *Nature Methods* **5**, 591–596 (2008). URL <https://doi.org/10.1038/nmeth.1221>.
- [4] Bogaerts, W. *et al.* Programmable photonic circuits. *Nature* **586**, 207–216 (2020). URL <https://doi.org/10.1038/s41586-020-2764-0>.
- [5] Chen, X., Lin, J. & Wang, K. A review of silicon-based integrated optical switches. *Laser & Photonics Reviews* **17**, 2200571 (2023).
- [6] Cheben, P., Halir, R., Schmid, J. H., Atwater, H. A. & Smith, D. R. Subwavelength integrated photonics. *Nature* **560**, 565–572 (2018). URL <https://doi.org/10.1038/s41586-018-0421-7>.
- [7] Zhang, L. *et al.* Ultralow-loss silicon photonics beyond the singlemode regime. *Laser & Photonics Reviews* **16**, 2100292 (2022).
- [8] Najjar Amiri, A., Vit, A. D., Gorgulu, K. & Magden, E. S. Deep photonic network platform enabling arbitrary and broadband optical functionality. *Nature Communications* **15**, 1432 (2024). URL <https://doi.org/10.1038/s41467-024-45846-3>.
- [9] Vit, A. D. *et al.* Universal on-chip polarization handling with deep photonic networks. *Journal of Lightwave Technology* **43**, 8770–8776 (2025).
- [10] Vit, A. D. *et al.* Layout-aware and fabrication-tolerant deep photonic networks. *J. Lightwave Technol.* **43**, 10841–10848 (2025). URL <https://opg.optica.org/jlt/abstract.cfm?URI=jlt-43-24-10841>.
- [11] Gorgulu, K., Vit, A. D., Amiri, A. N. & Magden, E. S. On-chip arbitrary dispersion engineering with deep photonic networks. *Opt. Lett.* **50**, 3780–3783 (2025). URL <https://opg.optica.org/ol/abstract.cfm?URI=ol-5-0-11-3780>.
- [12] Chang, L., Liu, S. & Bowers, J. E. Integrated optical frequency comb technologies. *Nature Photonics* **16**, 95–108 (2022). URL <https://doi.org/10.1038/s41566-021-00945-1>.
- [13] Grotevent, M. J. *et al.* Integrated photodetectors for compact fourier-transform waveguide spectrometers. *Nature Photonics* **17**, 59–64 (2023). URL <https://doi.org/10.1038/s41566-022-01088-7>.
- [14] Oktay, M. C., Gorgulu, K. & Magden, E. S. Computationally efficient nanophotonic design through data-driven eigenmode expansion. *Journal of Lightwave Technology* **42**, 7894–7902 (2024).
- [15] Oktay, M. C., Danis, B. S., Rzayev, U. & Magden, E. S. Experimental demonstration of ultra-wideband tapers, splitters and crossings with sub-0.1 db loss through computationally efficient and data-driven eigenmode expansion. In *2025 Conference on Lasers and Electro-Optics Europe & European Quantum Electronics Conference (CLEO/Europe-EQEC)*, 1–1 (2025).
- [16] Altindag, A., Dasdemir, A. O. & Magden, E. S. Experimental demonstration of a broadband, ultra-compact, and fabrication-tolerant silicon photonic 10% power tap. In Reed, G. T. & Knights, A. P. (eds.) *Silicon Photonics XIX*, vol. 12891, 128910R. International Society for Optics and Photonics (SPIE, 2024). URL <https://doi.org/10.1117/12.3002608>.
- [17] Dasdemir, A. O., Koral, A. K., Kiraz, B., Kiraz, A. & Magden, E. S. Multi-scale hierarchical topology optimization for nanophotonic design. In *OSA Advanced Photonics Congress (AP) 2020 (IPR, NP, NOMA, Networks, PVLED, PSC, SPPCom, SOF)*, ITu4A.11 (Optica Publishing Group, 2020). URL <https://opg.optica.org/abstract.cfm?URI=IPRSN-2020-ITu4A.11>.
- [18] Tran, M. A. *et al.* Extending the spectrum of fully integrated photonics to submicrometre wavelengths. *Nature* **610**, 54–60 (2022). URL <https://doi.org/10.1038/s41586-022-05119-9>.
- [19] Hinney, J. *et al.* Efficient excitation and control of integrated photonic circuits with virtual critical coupling. *Nature Communications* **15**, 2741 (2024). URL <https://doi.org/10.1038/s41586-024-05119-9>.

//doi.org/10.1038/s41467-024-46908-2.

[20] Wiecha, P. R., Arbouet, A., Girard, C. & Muskens, O. L. Deep learning in nano-photonics: inverse design and beyond. *Photon. Res.* **9**, B182–B200 (2021). URL <https://opg.optica.org/prj/abstract.cfm?URI=prj-9-5-B182>.

[21] Molesky, S. *et al.* Inverse design in nanophotonics. *Nature Photonics* **12**, 659–670 (2018). URL <https://doi.org/10.1038/s41566-018-0246-9>.

[22] MacLellan, B. *et al.* Inverse design of photonic systems. *Laser & Photonics Reviews* **18**, 2300500 (2024).

[23] Christiansen, R. E. & Sigmund, O. Inverse design in photonics by topology optimization: tutorial. *J. Opt. Soc. Am. B* **38**, 496–509 (2021). URL <https://opg.optica.org/josab/abstract.cfm?URI=josab-38-2-496>.

[24] Hughes, T. W., Minkov, M., Williamson, I. A. D. & Fan, S. Adjoint method and inverse design for nonlinear nanophotonic devices. *ACS Photonics* **5**, 4781–4787 (2018). URL <https://doi.org/10.1021/acsphotonics.8b01522>.

[25] Wang, K. *et al.* Inverse design of digital nanophotonic devices using the adjoint method. *Photon. Res.* **8**, 528–533 (2020). URL <https://opg.optica.org/prj/abstract.cfm?URI=prj-8-4-528>.

[26] Piggott, A. Y. *et al.* Inverse design and demonstration of a compact and broadband on-chip wavelength demultiplexer. *Nature Photonics* **9**, 374–377 (2015). URL <https://doi.org/10.1038/nphoton.2015.69>.

[27] Guo, M. *et al.* Advances in on-chip polarization multiplexing devices: From traditional designs to inverse design and hybrid multiplexing. *Laser & Photonics Reviews* **19**, e00643 (2025).

[28] He, W. *et al.* Ultrafast all-optical terahertz modulation based on an inverse-designed metasurface. *Photon. Res.* **9**, 1099–1108 (2021). URL <https://opg.optica.org/prj/abstract.cfm?URI=prj-9-6-1099>.

[29] Lin, S., Moazeni, S., Settaluri, K. T. & Stojanović, V. Electronic–photonic co-optimization of high-speed silicon photonic transmitters. *Journal of Lightwave Technology* **35**, 4766–4780 (2017).

[30] Yang, K. Y. *et al.* Multi-dimensional data transmission using inverse-designed silicon photonics and microcombs. *Nature Communications* **13**, 7862 (2022). URL <https://doi.org/10.1038/s41467-022-35446-4>.

[31] Lalau-Keraly, C. M., Bhargava, S., Miller, O. D. & Yablonovitch, E. Adjoint shape optimization applied to electromagnetic design. *Opt. Express* **21**, 21693–21701 (2013). URL <https://opg.optica.org/oe/abstract.cfm?URI=oe-21-18-21693>.

[32] Jensen, J. & Sigmund, O. Topology optimization for nano-photonics. *Laser & Photonics Reviews* **5**, 308–321 (2011).

[33] Hooten, S. *et al.* Automatic differentiation accelerated shape optimization approaches to photonic inverse design in fdtd/fdtd. *Laser & Photonics Reviews* **19**, 2301199 (2025).

[34] Schwab, J., Antholzer, S. & Haltmeier, M. Deep null space learning for inverse problems: convergence analysis and rates. *Inverse Problems* **35**, 025008 (2019). URL <https://doi.org/10.1088/1361-6420/aaf14a>.

[35] Zandehshahvar, M. *et al.* Manifold learning for knowledge discovery and intelligent inverse design of photonic nanostructures: Breaking the geometric complexity. *ACS Photonics* **9**, 714–721 (2022). URL <https://doi.org/10.1021/acsphotonics.1c01888>.

[36] Xu, X., Li, Y., Du, L. & Huang, W. Inverse design of nanophotonic devices using generative adversarial networks with the sim-nn model and self-attention mechanism. *Micromachines* **14**, 634 (2023). URL <https://www.mdpi.com/2072-666X/14/3/634>.

[37] Wong, J. J., Pesch, R. P., Hiesener, J. M. & Ralph, S. E. Simplifying photonic topologies in inverse design with contour constraints. *IEEE Photonics Technology Letters* **38**, 117–120 (2026).

[38] Piggott, A. Y., Petykiewicz, J., Su, L. & Vučković, J. Fabrication-constrained nanophotonic inverse design. *Scientific Reports* **7**, 1786 (2017). URL <https://doi.org/10.1038/s41598-017-01939-2>.

[39] Piggott, A. Y. *et al.* Inverse-designed photonics for semiconductor foundries. *ACS Photonics* **7**, 569–575 (2020). URL <https://doi.org/10.1021/acsphotonics.9b01540>.

[40] Hammond, A. M., Oskooi, A., Johnson, S. G. & Ralph, S. E. Photonic topology optimization with semiconductor-foundry design-rule constraints. *Optics Express* **29**, 23916–23938 (2021). URL <https://opg.optica.org/oe/abstract.cfm?URI=oe-29-15-23916>.

[41] Vercruyse, D., Sapra, N. V., Su, L., Trivedi, R. & Vučković, J. Analytical level set fabrication constraints for inverse design. *Scientific Reports* **9**, 8999 (2019). URL <https://doi.org/10.1038/s41598-019-45026-0>.

[42] Seo, D., Um, S., Lee, S., Ye, J. C. & Chung, H. Physics-guided and fabrication-aware inverse design of photonic devices using diffusion models. *ACS Photonics* **13**, 363–372 (2026). URL <https://doi.org/10.1021/acsphotonics.5c00993>.

[43] Chen, Y. *et al.* Inverse design of free-form devices with fabrication-friendly topologies based on structure transformation. *Journal of Lightwave Technology* **41**, 4762–4776 (2023).

[44] Hiesener, J. M., Kaylor, C. A., Wong, J. J., Agarwal, P. & Ralph, S. E. Seeded topology optimization for commercial foundry integrated photonics. *APL Photonics* **10** (2025). URL <http://dx.doi.org/10.1063/5.0287160>. Preprint available at <https://doi.org/10.48550/arXiv.2503.00199>.

[45] Schubert, M. F., Cheung, A. K. C., Williamson, I. A. D., Spyra, A. & Alexander, D. H. Inverse design of photonic devices with strict foundry fabrication constraints. *ACS Photonics* **9**, 2327–2336 (2022). URL <https://doi.org/10.1021/acsphotonics.2c00313>.

[46] Tang, Y. *et al.* Generative deep learning model for inverse design of integrated nanophotonic devices. *Laser & Photonics Reviews* **14**, 2000287 (2020).

[47] Chen, H., Zhang, M. & Tong, Y. Always-feasible photonic inverse design with a differentiable conditional design generator. *ACS Photonics* **11**, 4461–4471 (2024). URL <https://doi.org/10.1021/acsphotonics.4c01522>.

[48] Bengio, Y., Léonard, N. & Courville, A. Estimating or propagating gradients through stochastic neurons for conditional computation. *arXiv preprint arXiv:1308.3432* (2013). URL <https://arxiv.org/abs/1308.3432>. 1308.3432.

[49] Caseman, R. noise (version 1.2.2) [python package]. <https://github.com/caseman/noise> (2015). Accessed: 2026-01-29.

[50] Hughes, T. W., Williamson, I. A. D., Minkov, M. & Fan, S. Forward-mode differentiation of maxwell's equations. *ACS Photonics* **6**, 3010–3016 (2019). URL <https://doi.org/10.1021/acsphotonics.9b01238>.

[51] Schubert, F. *et al.* Quantized inverse design for photonic integrated circuits. *ACS Omega* **10**, 5080–5086 (2025). URL <https://doi.org/10.1021/acsomega.4c10958>.

[52] Tang, R. J., Lim, S. W. D., Ossianer, M., Yin, X. & Capasso, F. Time reversal differentiation of fdtd for photonic inverse design. *ACS Photonics* **10**, 4140–4150 (2023). URL <https://doi.org/10.1021/acsphotonics.3c00694>.

[53] Dasdemir, A. O., Minden, V. & Magden, E. S. Computational scaling in inverse photonic design through factorization caching. *Applied Physics Letters* **123**, 221106 (2023). URL <https://doi.org/10.1063/5.0172019>.

[54] Michaels, A. & Yablonovitch, E. Leveraging continuous material averaging for inverse electromagnetic design. *Opt. Express* **26**, 31717–31737 (2018). URL <https://optica.org/oe/abstract.cfm?URI=oe-26-24-31717>.

[55] Guest, J. K., Prévost, J. H. & Belytschko, T. Achieving minimum length scale in topology optimization using nodal design variables and projection functions. *International Journal for Numerical Methods in Engineering* **61**, 238–254 (2004).

[56] Heek, J. *et al.* Flax: A neural network library and ecosystem for jax. GitHub software, version 0.12.0 (2024). URL <http://github.com/google/flax>.

[57] Bradbury, J. *et al.* Jax: Composable transformations of python+numpy programs. GitHub software, version 0.3.13 (2018). URL <http://github.com/jax-ml/jax>.

[58] Babuschkin, I. *et al.* The DeepMind JAX ecosystem. Software available at <http://github.com/google-deepmind> (2020).

[59] Johnson, S. G. The NLOpt nonlinear-optimization package. Software available at <http://github.com/stevengj/nlopt> (2024).

[60] Intel Corporation. oneMKL PARDISO: Parallel direct sparse solver interface. <https://software.intel.com/content/www/us/en/develop/tools/oneapi/components/onemkl.html> (2023). Accessed 29 Jan 2026.

Intrinsically DRC-Compliant Nanophotonic Design via Learned Generative Manifolds: Supporting Information

Bahrem Serhat Danis,¹ Demet Baldan Desdemir,¹ Enes Akcakoca,¹ Zeynep Ipek Yanmaz,¹ Gulzade Polat,¹ Ahmet Onur Dasdemir,¹ Aytug Aydogan,² Abdullah Magden,³ and Emir Salih Magden^{1,4,*}

¹*Dept. of Electrical and Electronics Engineering, Koç University, Istanbul, 34450, Turkey*

²*KU Leuven, Dept. of Physics and Astronomy, B-3000 Leuven, Belgium*

³*Dept. of Mathematics, Faculty of Engineering and Natural Sciences, Bursa Technical University, Bursa, 16310, Turkey*

⁴*KUIS AI, Koç University, Istanbul, 34450, Turkey*

I. TOPOLOGICAL LOSS FUNCTION

The topological loss term [1] is designed as a combination of two distinct design-rule constraints corresponding to the minimum linewidth and minimum line spacing. It serves to enforce manufacturability constraints during the optimization process by penalizing structural features that violate these design rules

$$\mathcal{L} = \sum_{i,j} I_{i,j}^{\text{LW}}(\rho) [\min(\rho_{i,j} - \eta_e, 0)]^2 + I_{i,j}^{\text{LS}}(\rho) [\min(\eta_d - \rho_{i,j}, 0)]^2. \quad (1)$$

Here, ρ denotes the normalized permittivity profile ranging from 0 (SiO_2) to 1 (Si). The parameters η_d and η_e act as threshold values that govern the dilation and erosion steps, respectively. Two auxiliary indicator functions, I_{LW} and I_{LS} , are then constructed to identify the silicon and silica domains based on these thresholded regions.

$$I^{\text{LW}}(\rho, \tilde{\rho}) = \tilde{\rho} \exp(-\alpha|\nabla\rho|^2) \quad (2)$$

$$I^{\text{LS}}(\rho, \tilde{\rho}) = (1 - \tilde{\rho}) \exp(-\alpha|\nabla\rho|^2) \quad (3)$$

In this formulation, $\tilde{\rho}$ represents the generator output after applying a 2D Gaussian blur with radius R , while α controls the relative contribution of the two auxiliary indicators. The threshold parameters η_d and η_e are linked to the minimum linewidth l_w , minimum line spacing l_s , and the Gaussian filter radius, since violations of these design rules are detected through the filtering process. As the filter radius determines the effective smoothing scale, its relation to l_w and l_s dictates how these thresholds are selected. Therefore, η_d and η_e intrinsically depend on l_w , l_s , and R . During training, the topological loss incorporates indicator functions that identify inflection regions and exploit the known relationship between the filter kernel and the morphological transformations, specifically the erode and dilate operations, thereby guiding the generator toward designs that rigorously satisfy geometric constraints.

* Corresponding author: esmagden@ku.edu.tr

The threshold parameters η_d and η_e are determined directly from the foundry-specified minimum linewidth (l_w) and minimum spacing (l_s), following the methodology outlined in previous studies [1, 2]. These studies emphasized that maintaining strict control over the smallest permissible feature widths and gap distances is essential for preventing numerical artifacts and ensuring smooth, fabrication-consistent topologies in the optimization process:

$$\eta_e = \begin{cases} \frac{1}{4} \left(\frac{l_w}{R} \right)^2 + \frac{1}{2}, & \frac{l_w}{R} \in [0, 1], \\ -\frac{1}{4} \left(\frac{l_w}{R} \right)^2 + \frac{l_w}{R}, & \frac{l_w}{R} \in [1, 2], \\ 1, & \frac{l_w}{R} \in [2, \infty). \end{cases} \quad (4)$$

$$\eta_d = \begin{cases} \frac{1}{2} - \frac{1}{4} \left(\frac{l_s}{R} \right)^2, & \frac{l_s}{R} \in [0, 1], \\ 1 + \frac{1}{4} \left(\frac{l_s}{R} \right)^2 - \frac{l_s}{R}, & \frac{l_s}{R} \in [1, 2], \\ 0, & \frac{l_s}{R} \in [2, \infty). \end{cases} \quad (5)$$

These specific values are determined from the ratio of the minimum linewidth to the minimum spacing, ensuring accurate thresholding, allowing the correct identification of regions that violate the design rules for linewidth and line spacing. Following the methodology in previous studies[1, 3, 4], we use $l_s = l_w$ and set the Gaussian filter radius to twice the minimum feature size, $R = 2l_w = 2l_s$, which corresponds to typical values reported in the literature. Under these conditions, the threshold parameters are assigned as $\eta_e = 0.75$ and $\eta_d = 0.25$. In our generator implementation, the minimum linewidth and spacing are explicitly defined according to the fabrication process. For the standard electron-beam lithography (EBL) generator model, the minimum feature size is set to 60 nm, resulting in a Gaussian filter radius of 120 nm. For the photolithography (PL) generator model, the minimum feature size is 150 nm, with a corresponding filter radius of 300 nm. This configuration ensures that the topological loss accurately reflects process-specific fabrication limits while maintaining consistent morphological control. In addition, the damping coefficient α is defined as the fourth power of the grid resolution, $\alpha = (1/25 \text{ nm})^4 = 2.56 \times 10^{-6} \text{ nm}^{-4}$. This value is sufficient for these hyperparameters to accurately detect regions where the linewidth constraints are violated.

II. TRAINING LATENT SPACE DATASET WITH SPATIAL FEATURE DIVERSITY

To ensure that the training dataset encompasses samples capturing both coarse and fine spatial features, we generated 1,000 unique noise patterns. This diverse dataset is crucial for minimizing overfitting and maximizing the model's generalizability across varied latent space inputs. Mathematically, each training sample $I(x, y)$ is constructed as a superposition of D independent noise components, η_d , with each modulated by distinct scale (s) and offset (O_x, O_y) parameters.

$$I(x, y) = \frac{1}{D} \sum_{d=1}^D \eta_d \left(\frac{x + O_x}{s}, \frac{y + O_y}{s} \right), \quad (6)$$

This construction allows us to synthesize a broad spectrum of structural complexity, thoroughly exploring the feature space of the latent representation. The core of this synthesis lies in the scale parameter s , which directly controls the frequency content of the noise: larger values generate low-frequency, coarse features, while smaller values produce high-frequency, fine details. Concurrently, the offset parameters O_x and O_y introduce translational shifts to the pattern, effectively sampling different phase spaces of the noise field. By averaging over D independent fields, we achieve a statistically robust and richer combination of features, far surpassing simple random sampling. The d -th stochastic noise field, $\eta_d(u, v)$, is defined by a pseudo-random gradient interpolation function, which ensures the generated noise possesses perceptually coherent, continuous structures rather than being uniform white noise. The field is mathematically defined using a summation over grid points (i, j) :

$$\eta_d(u, v) = \sum_{i=0}^1 \sum_{j=0}^1 w_i(u) w_j(v) \mathbf{g}_{d,ij} \cdot (u - i, v - j). \quad (7)$$

Here, $\mathbf{g}_{d,ij}$ are pseudo-random gradient vectors assigned at each lattice point (i, j) ; $w_i(u)$ is the smooth fade (interpolation) function; (x, y) are pixel coordinates in the 2D spatial domain; s is the scale controlling spatial frequency; (O_x, O_y) are spatial offsets introducing positional shifts; and D is the number of independent noise channels controlling structural complexity. Finally, each noise map is normalized to the unit interval as:

$$I'(x, y) = \frac{I(x, y) - \min(I)}{\max(I) - \min(I)}. \quad (8)$$

This formulation explicitly defines the generation process used by the `noise` library[5], ensuring reproducible construction of noise fields with tunable spatial diversity across multiple scales and offsets. We generated 1,000 samples by systematically varying the scale, offset, and noise dimensionality. These variations produced multiple granularities across different topologies, thereby enhancing the generalization capabilities of the generator. Specifically, the scale parameter modulates the spatial frequency of the noise, controlling whether the resulting patterns exhibit fine or coarse textures. The offset introduces spatial shifts, allowing the generator to encounter diverse spatial alignments. The noise dimensionality defines the number of independent stochastic components shaping each pattern, thereby

modulating structural complexity and diversity.

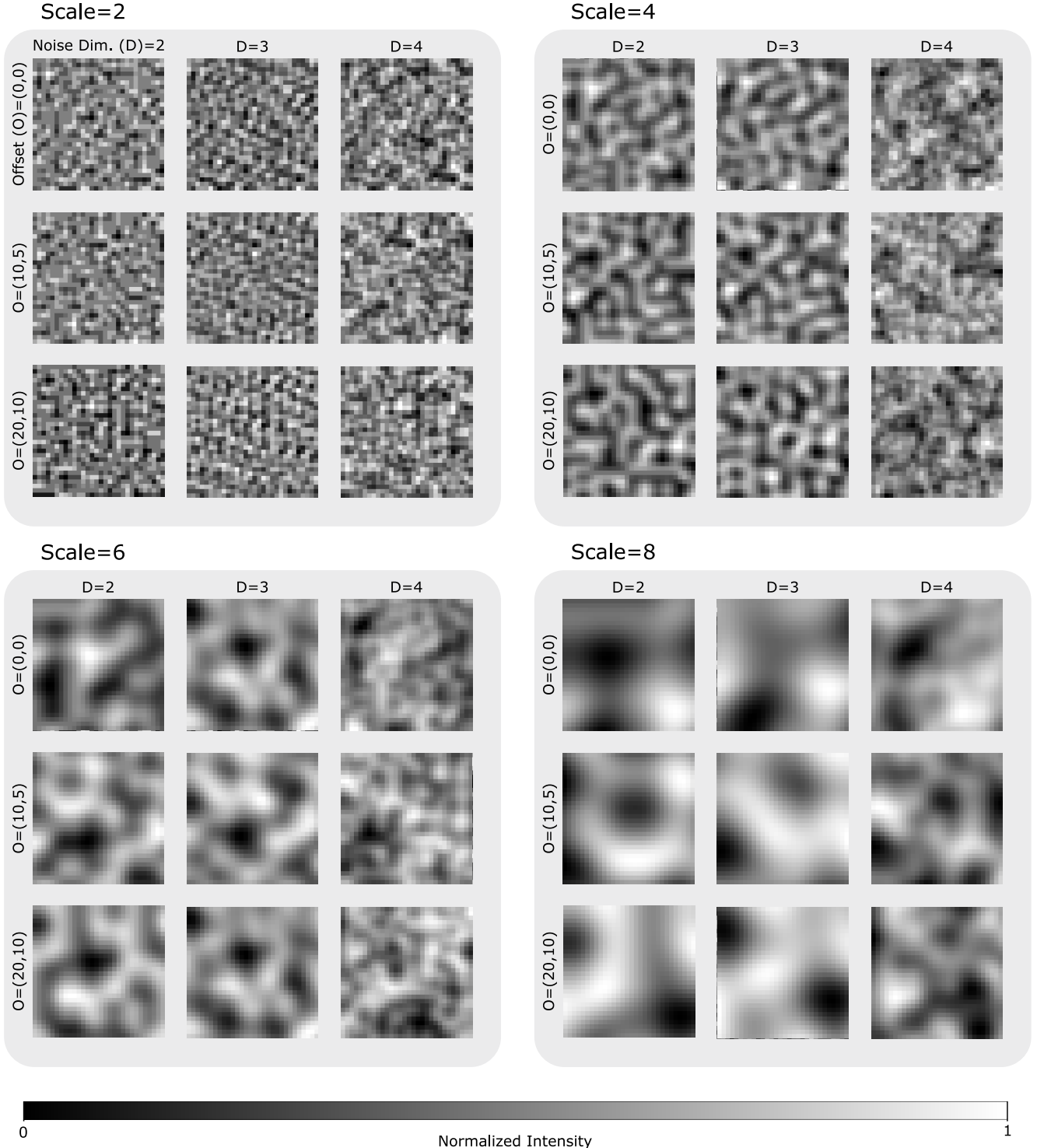


FIG. S1. Effect of noise hyperparameters on spatial features. Two-dimensional noise maps (30×30 pixels) were generated by varying the scale (2, 4, 6, 8), offset (O) = (0, 0), (10, 5), (20, 10), and noise dimensionality (D) = 2, 3, 4. Increasing the scale smooths the spatial features, while higher dimensionality introduces finer variations. These maps represent representative latent-space samples used for training the electron-beam lithography and photolithography generator models. Grayscale denotes normalized intensity from 0 (black) to 1 (white).

To show the effect of noise hyperparameters on spatial features, we varied the scale, offset, and dimensionality for a fixed 30×30 2D noise map. As can be seen from Fig. S1, the scale takes values 2, 4, 8, and 16; offsets are set as integer pairs such as $(0, 0)$, $(10, 5)$, and $(20, 10)$; and the noise dimensionality is 2, 3, or 4. This figure illustrates how spatial features change under fixed input conditions.

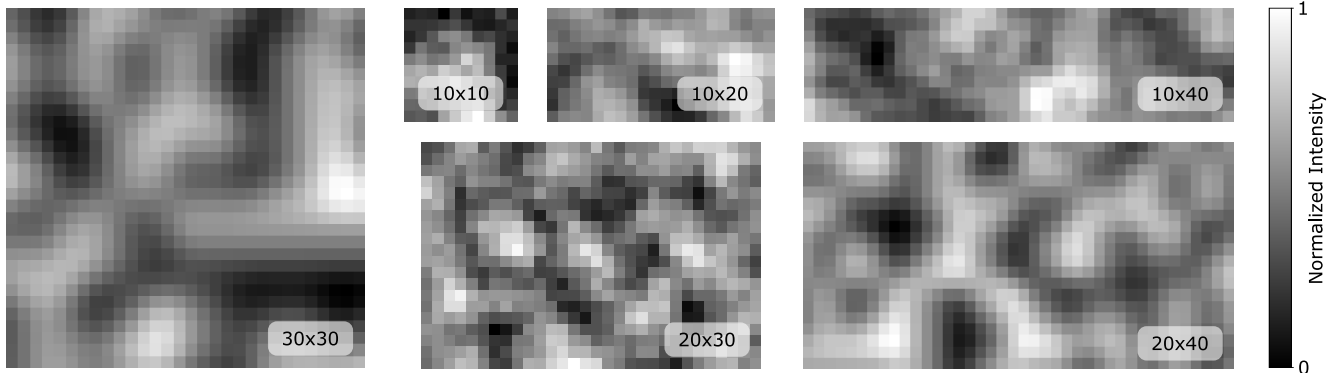


FIG. S2. Representative training samples of varying sizes generated under different noise hyperparameter settings. The multi-scale latent space realizations, changing latent dimensions from 10×10 to 30×30 pixels, illustrate how variations in latent space size and noise hyperparameters shape the normalized intensity distributions.

During sample generation, the scale parameter was randomly selected as an integer between 2 and 16. Offsets were chosen as random integer pairs, with minimum values of 0 and maximum values determined by the corresponding sample dimensionality. The noise dimensionality was randomly selected as 2, 3, or 4 for each sample. Additionally, to enable the training of a size-agnostic generator capable of producing layouts of various dimensions, the sample size was randomly assigned as an integer between 4 and 45, independently for both x and y dimensions. Samples generated from the training latent space dataset, each using randomly picked noise hyperparameters, can be seen in Fig. S2. Fig. S2 specifically illustrates the variety of sample dimensions (e.g., 30×30 , 10×10 , 10×20 , 10×40 , 20×30 , and 20×40 pixels) used in the training dataset to achieve the size-agnostic capability. This extensive variation in the input dimensions ensures the model learns the underlying latent relationships independently of the fixed output size. Consequently, the generator is robustly trained across a wide range of dimensionality, allowing it to generalize effectively when generating patterns for arbitrary x and y dimensions not seen during training.

III. INPUT-OUTPUT SIZE MAPPING IN THE ELECTRON-BEAM AND PHOTOLITHOGRAPHY GENERATOR MODELS

The input space of the model consists of grayscale two-dimensional distributions with pixel intensities normalized within the range $[0, 1]$. The minimum input dimension is 4×4 , while the maximum size can be arbitrarily chosen depending on the desired spatial scale. In our training, the grayscale latent-space samples were generated up to 60×60 pixels. Since both generator models are composed entirely of convolutional layers followed by pointwise nonlinear functions, they are inherently size-agnostic. This means that the same model architecture can process inputs of arbitrary spatial dimensions, effectively allowing the generation of physically larger patterns without structural modification. The mapping between the input and output sizes exhibits an approximately linear relationship; each input pixel corresponds to a predictable number of output pixels, enabling one-dimensional interpolation of the scaling behavior. For the EBL generator, the effective scaling factor is approximately 11, while for the PL generator, it is around 18. However, due to discrete convolution operations involving floor rounding, the mapping is not perfectly linear.

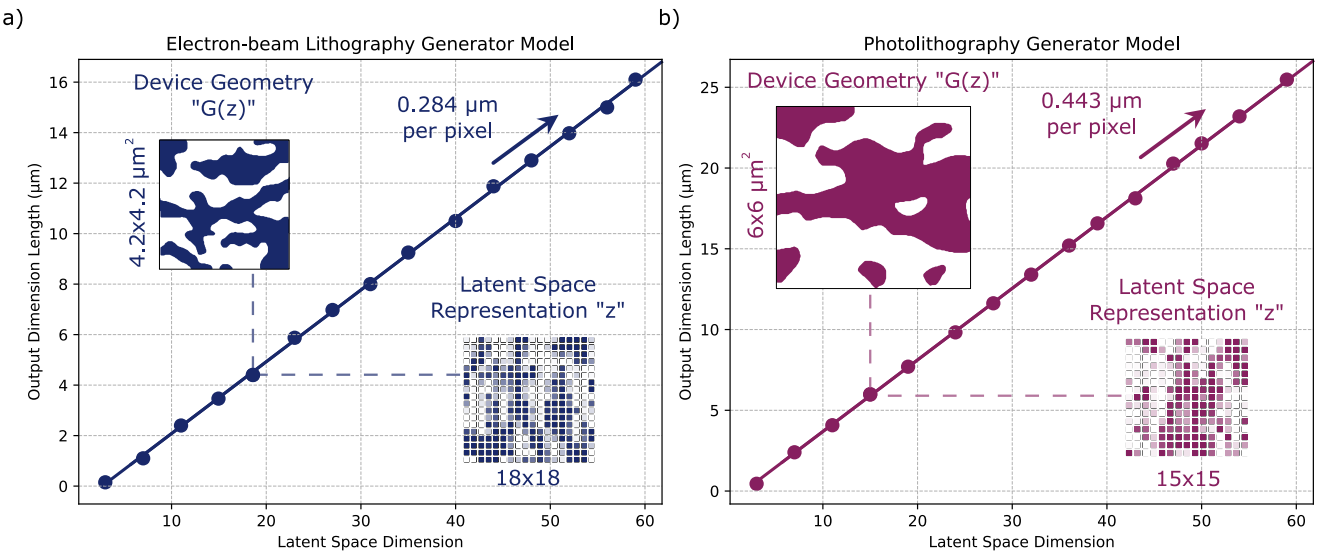


FIG. S3. Latent-space interpolation and physical mapping for EBL and PL generators. (a) EBL generator and (b) PL generator: interpolation of latent-space dimensions to physical output dimensions. Insets: top-left, representative latent-space vector; bottom-right, corresponding output structure from the trained generator, with indicated physical dimensions. The comparison highlights the distinct spatial resolutions: the EBL generator produces high-resolution outputs ($\sim 0.284 \mu\text{m}/\text{pixel}$ equivalent), whereas the PL generator yields coarser patterns ($\sim 0.443 \mu\text{m}/\text{pixel}$).

Both generator outputs are defined on a geometrical grid resolution of 25 nm in the space of the device geometry. As shown in Fig. S3, after interpolation, a single latent-space pixel represents approximately 30 nm in the device space of the EBL generator and 50 nm in that of the PL generator. This difference highlights the distinct spatial resolutions of the two models: the EBL generator produces high-resolution patterns ($\approx 0.284 \mu\text{m}/\text{pixel}$ equivalent), whereas the PL generator operates at a lower resolution ($\approx 0.443 \mu\text{m}/\text{pixel}$). Fig. S3 insets illustrate the translation of a shared latent-space input into the respective physical domains of each generator. Each model produces geometries tailored to its specific fabrication regime, ensuring that the resulting structures satisfy the inherent resolution limits and design rules of either EBL or PL.

IV. DISCRETENESS METRIC Γ FOR MONITORING BINARIZATION AND PROJECTION STRENGTH PARAMETER β

To quantitatively assess how well the material boundaries between SiO_2 and Si are defined in the design region, we define a discreteness metric (Γ) that measures how close each design pixel (or voxel) is to the two binary material states (0 for SiO_2 , and 1 for Si). This metric provides an interpretable scalar measure of how closely the density distribution $\rho(x, y) \in [0, 1]$ approaches a binary state. Here, $\Gamma = 1$ corresponds to a completely binarized structure and $\Gamma = 0$ represents a fully grayscale distribution. While the metric is applicable to any two-material system, the values $\rho(x, y) = 0$ and $\rho(x, y) = 1$ in this study specifically represent the SiO_2 and Si phases. Intermediate values denote partially mixed or non-binarized regions.

To compute the discreteness, the design region is first divided into $N_x \times N_y$ subregions denoted by $\Omega_{i,j}$, where $i = 1, 2, \dots, N_x$ and $j = 1, 2, \dots, N_y$. The subregion division ensures that the metric captures spatial variations in binarization across the entire structure. For each subregion $\Omega_{i,j}$, the local discreteness value $\Gamma_{i,j}$ is defined as the ratio of pixels whose density values fall within a discrete tolerance range near 0 or 1, relative to the total number of pixels in that subregion:

$$\Gamma_{i,j} = \frac{N_{\text{discrete}}^{(i,j)}}{N_{\text{total}}^{(i,j)}} \quad (9)$$

where

$$N_{\text{discrete}}^{(i,j)} = \# \{ \rho(x, y) \in \Omega_{i,j} \mid \rho(x, y) \leq \tau \text{ or } \rho(x, y) \geq 1 - \tau \}. \quad (10)$$

Here, τ is the discreteness tolerance parameter (typically set between 0.01 and 0.05) that determines how close a pixel's value must be to either binary state to be considered discrete. For the pixel-based optimization performed in the main text, we set $\tau = 0.01$. $N_{i,j}^{\text{total}} = |\Omega_{i,j}|$ denotes the total number of pixels in the subregion. The overall discreteness of the structure is obtained by averaging the local values over all subregions:

$$\Gamma = \frac{1}{N_x N_y} \sum_{i=1}^{N_x} \sum_{j=1}^{N_y} D_{i,j} \quad (11)$$

A higher value of Γ indicates that most of the design pixels have converged toward binary values, meaning the device is closer to a manufacturable topology with well-defined material boundaries. Conversely, a lower Γ signifies that a significant portion of the structure remains in an intermediate, non-binary state.

For the conventional optimization, we initialize the projection strength parameter β at 8. As illustrated in Fig. S1(a), whenever the optimization does not achieve sufficient improvement, we double the value of β , leading to an exponential increase. This strategy guarantees that the final design is fully binarized. The loss curve reveals that each increase in β initially raises the loss due to sudden changes in design parameters, while simultaneously improving the discreteness metric. The discreteness metric Γ quantifies the degree to which the design is binary or grayscale. Therefore, as β increases, the minimum achievable loss also worsens, indicating that the optimization problem becomes progressively more challenging.

V. TRAINING THE PHOTOLITHOGRAPHY GENERATOR MODEL

The PL generator model differs from the EBL generator model in two principal aspects. First, the overall upsampling ratio in the cascaded upsampling stages was increased from 1.4 to 1.6, resulting in a total latent-space scaling factor change from 1.4^4 to 1.6^4 . Second, the convolutional architecture was streamlined: the number of convolutional layers was reduced from three to two, while the kernel size was enlarged from 5×5 to 7×7 . This modification allows the network to better enforce design-rule constraints at larger feature scales. Additionally, the kernel size of the final morphological closing operation was expanded from 3×3 to 7×7 to ensure smoother feature boundaries and improved mask continuity.

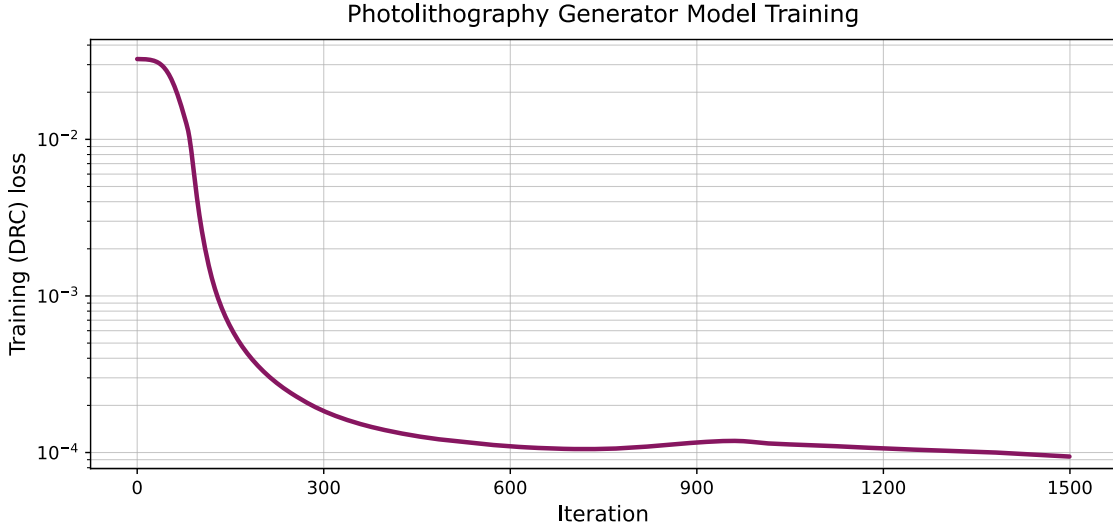


FIG. S4. Training dynamics of the photolithography generator. The design rule check loss decreases from $\sim 3 \times 10^{-2}$ to $\sim 1 \times 10^{-4}$ over 1500 iterations, showing a rapid reduction in the first 300 iterations and a gradual approach to saturation, indicating stable convergence of the model.

For training, we employed the same dataset used in the EBL generator model, ensuring a consistent comparison. Optimization was performed using the Adam optimizer, with hyperparameters identical to those reported in the Methods section. The training loss evolution for the PL generator is shown in Supplementary Fig. S4, where the design rule check (DRC) loss begins at approximately 3×10^{-2} and rapidly decreases during the first 300 iterations, reaching a near-saturation regime. By around 1500 iterations, the DRC loss converges to approximately 10^{-4} . This progressive reduction correlates with a gradual decrease in the number of DRC violations across generated device layouts. A DRC loss value on the order of 10^{-4} indicates a well-constrained design region with a minimum feature size of about 150 nm. Compared to the electron-beam generator, which achieves a minimum DRC loss of roughly 8×10^{-6} , the slightly higher final loss in the PL model originates from the larger Gaussian filter radius used during training. Increasing the filter size effectively enlarges the minimum allowable feature size in the topology, thereby increasing the norm of the gradients within the indicator functions. Consequently, the achievable minimum loss becomes bounded from below by this feature-size scaling. Moreover, the total number of trainable parameters in the PL generator was substantially reduced, from 13,243 in the electron-beam model to 1,619, leading to a shorter training duration of 1,500 iterations (compared to 2,060 iterations in the electron-beam case). This reduction accelerates convergence while preserving sufficient model expressivity for mask generation under photolithographic constraints.

VI. DEVICES DESIGNED WITH THE PHOTOLITHOGRAPHY MODEL AND THEIR OPTIMIZATION DETAILS

Using the PL-based generator model, we optimized the same three representative classes of photonic devices: power splitters, a photonic duplexer, and a mode converter. The simulation parameters, including the wavelength range, the Si/SiO₂ material platform, input light polarization, and the input–output waveguide widths, are kept identical to those used in the EBL configuration to ensure a fair comparison. Following optimization, each device design is subjected to an automated DRC, and all designs successfully passed without any violations. To translate these optimized designs into physically realizable patterns, the generator’s inference stage plays a crucial role. During the inference of the trained generator, the scheduled softmax is replaced with a thresholding operation to obtain a binary layout. Since this thresholding layer is non-differentiable, its gradient is approximated using the straight-through estimator introduced earlier, allowing the entire generator and pipeline to remain differentiable and enabling gradient-based optimization of the latent space. The results and performance analyses of these three device categories are reported in the following sections.

A. Broadband Power Splitters with Variable Splitting Ratios

Following the same design strategy as in the EBL model, three distinct power splitters are designed, each targeting a different splitting ratio. For all designs, the optimization process is performed using six discrete wavelength sampling points. The desired output power distributions are set to 50/50, 30/70, and 10/90 between the two output waveguides across the sampled wavelengths. Each optimized power splitter occupies a compact footprint of $6 \times 6 \mu\text{m}^2$.

For the 50/50 power splitter (Fig. S5(a)), the optimization process rapidly reduces the loss from 1.9 to 2×10^{-3} within 150 iterations, resulting in a well-balanced power distribution between the two output ports. As shown in Fig. S1(d), both the generator-based and conventional designs maintain transmission levels of 45–50% at each port over the wavelength range of 1,500–1,600 nm. The optimized splitter exhibits an overall transmission of 97%, corresponding to an insertion loss of 0.12 dB, demonstrating highly efficient power division. For the 30/70 power splitter, the optimization was performed using five sampling points, targeting 30% transmission at the top port and 70% at the bottom port. As shown in Fig. S5(b), the loss decreases from 1.38 to 1×10^{-3} after 150 iterations. The final device yields 27–29% transmission at the top port and 67–68% at the bottom port, achieving an insertion loss of approximately 0.11 dB at 1,550 nm. In the case of the 10/90 power splitter, six wavelength sampling points were used, targeting 10% transmission at the top port and 90% at the bottom port. The optimization converges after 150 iterations, reducing the loss from 1.52 to 1.27×10^{-3} (Fig. S5(c)). As illustrated in Fig. S5(d), the resulting device provides 7–8% transmission at the top port and 85–87% at the bottom port, corresponding to an insertion loss of about 0.09 dB. In all three optimization cases, convergence occurs around 150 iterations, indicating consistent optimization dynamics across the devices. This behavior is attributed to the identical latent space dimensionality used for all configurations. The final geometries of the optimized 50/50, 30/70, and 10/90 power splitters are displayed in Fig. S5(g)–Fig. S5(i), together with the normalized magnetic field distributions obtained from finite-difference frequency-domain (FDFD) simulations at 1,500, 1,550, and 1,600 nm.

The transition from the EBL generator model to the PL generator model necessitates a strategic footprint expansion

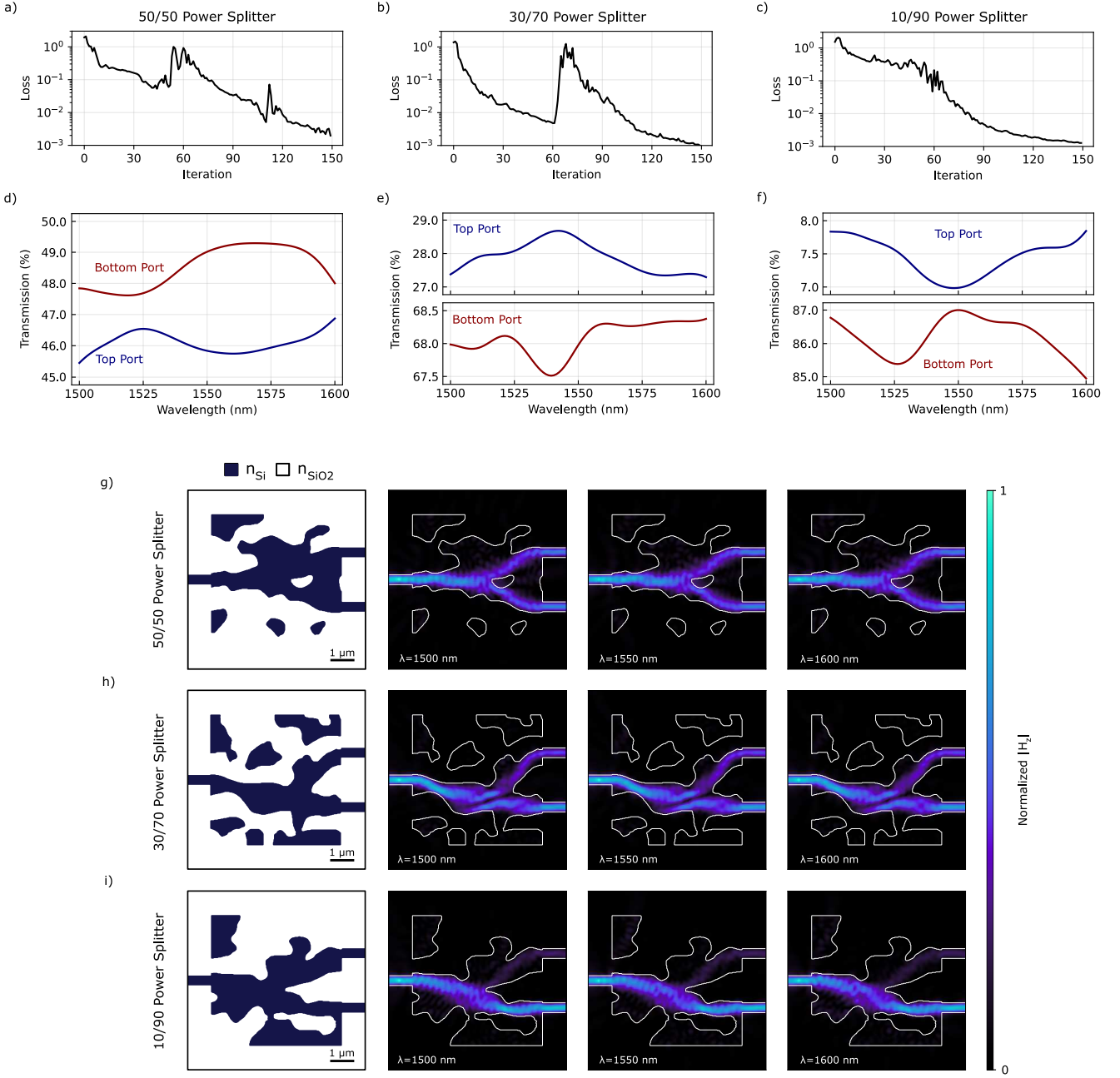


FIG. S5. Ultrabroadband power splitter performance for different splitting ratios designed with the photolithography generator model. (a)–(c) Evolution of the optimization loss during the training of the photolithography generator model for 50/50 (a), 30/70 (b), and 10/90 (c) power splitters, illustrating rapid reduction in loss across 150 iterations. (d)–(f) Spectral transmission for the top and bottom ports of the respective devices, showing consistent splitting behavior over the 1500–1600 nm wavelength range. (g)–(i) Left panels depict the final permittivity maps (silicon in dark blue, n_{Si} ; SiO_2 in white, n_{SiO_2}), while the right panels show the corresponding normalized magnetic field (H_z) distributions at $\lambda = 1500$, 1550, and 1600 nm. The field profiles confirm ultrabroadband operation across all splitter designs.

from $4.2 \times 4.2 \mu\text{m}^2$ to $6 \times 6 \mu\text{m}^2$. For the 50/50 power splitter, the EBL generator model achieves a loss of 3.2×10^{-4} within 150 iterations, while the PL generator model converges to 2×10^{-3} in the same number of iterations. Despite stricter constraints, the PL-based 50/50 power splitter maintains a 97% overall transmission and a low insertion loss of 0.12 dB. This indicates that increasing the design area can partially offset the limitations imposed by a

larger minimum feature size. The 30/70 power splitter further highlights the efficiency trade-offs between fabrication regimes. While both models converge within 150 iterations, the EBL generator model reaches a loss of 5×10^{-4} with a 0.11 dB insertion loss. Conversely, the PL generator model stabilizes at 1×10^{-3} and exhibits a significantly higher insertion loss of 0.5 dB at 1,550 nm. Despite this efficiency penalty, the device achieves the desired power distribution (27–29% top port transmission, and bottom port transmission), proving the generator’s ability to meet functional targets even when fine-grained topological features are restricted. In the high-contrast 10/90 power splitter case, optimization dynamics remain consistent, with both models reaching local minima after 150 iterations. The EBL generator model achieves a minimum loss of 4×10^{-4} (0.09 dB insertion loss), outperforming the PL generator model, which stabilizes at 1.27×10^{-3} with a 0.5 dB insertion loss. The resulting 85–87% bottom-port transmission for the PL design confirms the expected target operation. Ultimately, these small differences in performance are rooted in the reduced “designable” density of the parametrized manifold. The transition from an 18×18 latent space vector in the EBL generator model to a restricted 15×15 latent space vector in the PL generator model limits the available degrees of freedom. With fewer tunable parameters to satisfy electromagnetic boundary conditions, the optimization task becomes inherently more challenging. This necessitates the footprint expansion, accounts for the higher local minima, and explains the increased insertion loss observed in the PL generator model designs.

B. Multi-Wavelength Photonic Duplexer

A broadband wavelength duplexer was designed using the PL-based generator model to achieve efficient spectral routing within the 1,500–1,600 nm wavelength range. The device directs optical signals between 1,500 and 1,550 nm to the upper output port and those between 1,550 and 1,600 nm to the lower port, thereby functioning as a short-pass and long-pass splitter, respectively. The total device footprint is $10.5 \times 10.5 \mu\text{m}^2$. For optimization, we select ten discrete wavelengths within the 1,500–1,600 nm range. Five wavelengths evenly distributed from 1,500 to 1,550 nm target 100% transmission toward the top port, while the remaining five wavelengths between 1,550 and 1,600 nm target 100% transmission to the bottom port.

Following 250 optimization iterations, the loss value decreased substantially from 1.74 to 8.7×10^{-2} , as presented in Fig. S6(a). As shown in Fig. S6(b), the optimized device exhibits clear spectral separation between the two output channels, with an achieved transmission efficiency of approximately 94%, corresponding to an insertion loss of only 0.3 dB. The resulting geometry delineates the spatial distribution of Si and SiO₂ regions and successfully passes DRC. Fig. S6(c) depicts the normalized FDFD magnetic field distributions at 1,500, 1,550, and 1,600 nm, illustrating the wavelength-dependent routing behavior and confirming the duplexing performance of the device.

The performance differences between the PL-based and EBL generator models highlight the critical trade-off between fabrication constraints and device optimality. While the PL model optimized through 250 iterations, it reached a minimum loss of only 8.7×10^{-2} . On the other hand, the EBL model achieved a superior loss of 1×10^{-2} within 160 iterations. This performance gap is primarily attributed to the differences in the dimensionality of the latent space and the resulting feature size limitations. As the device exhibits a wavelength-dependent response, its performance is highly sensitive to subtle geometric variations that govern interference and phase accumulation across the structure. The PL model utilizes a 24×24 latent space grid, which provides fewer degrees of freedom compared to the 28×28 latent space employed by the EBL model. This reduced spatial resolution restricts the generator-based optimization

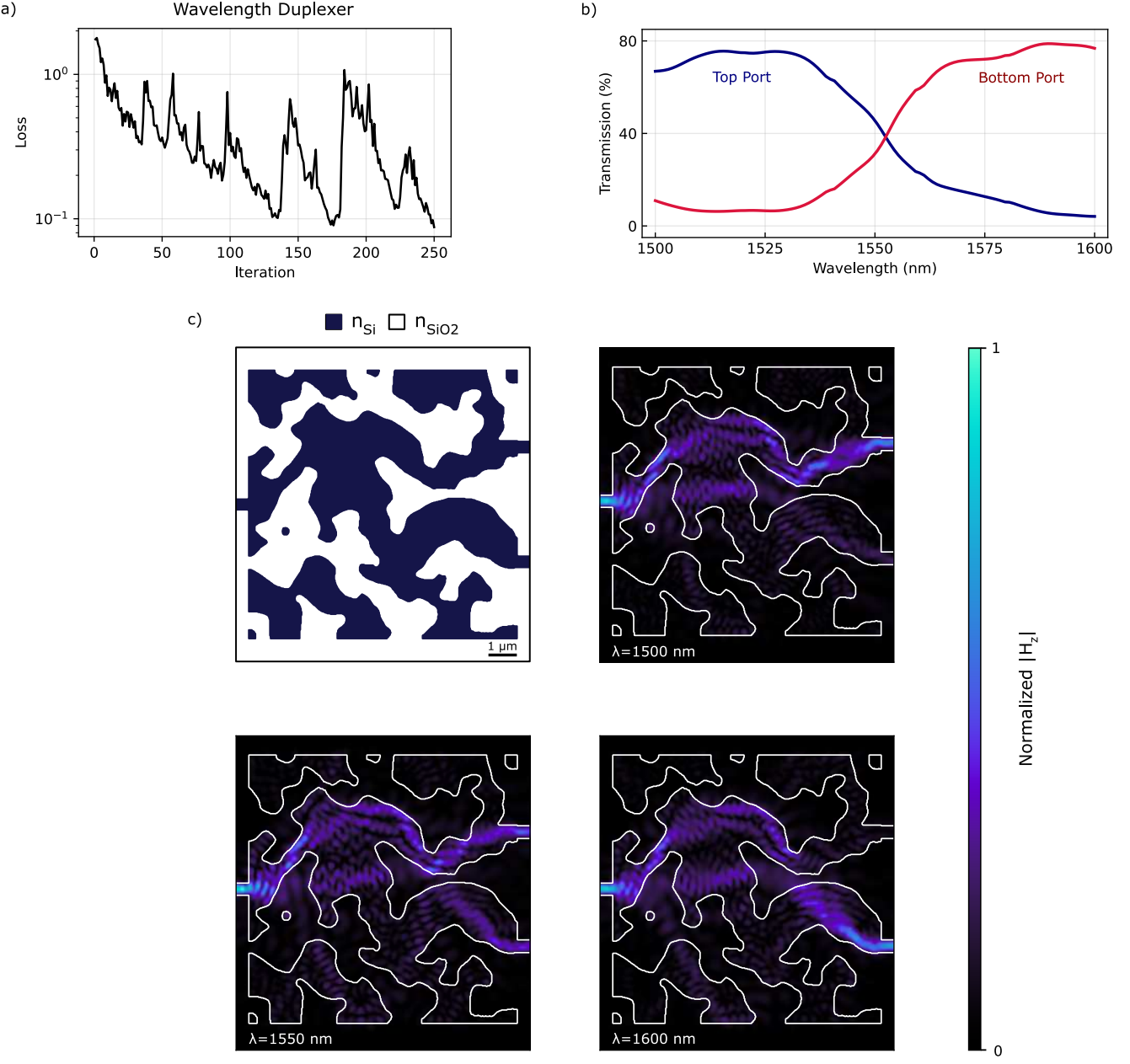


FIG. S6. Multi-wavelength photonic duplexer optimized with an electron-beam-lithography-compliant generator. (a) Evolution of the optimization loss over 250 iterations, showing a significant drop from 1.74 to 8.7×10^{-2} . (b) Transmission spectra of the final device, illustrating effective separation between the top and bottom ports with a peak transmission of $\sim 94\%$, corresponding to an insertion loss of 0.3 dB. (c) Final layout of the device (top left), with silicon regions in dark blue and SiO_2 in white, fully complying with design rule constraints. The adjacent panels display normalized FDFD magnetic field distributions at 1500 , 1550 , and 1600 nm, demonstrating consistent wavelength-dependent routing and confirming the duplexing performance.

capacity to encode fine geometric modulations necessary for shaping wavelength-dependent field distributions, leading to a degraded spectral response. This reduction in the optimized spatial degrees of freedom significantly decreases the tunability of the device geometry. Furthermore, the increased feature size (from 60 nm to 150 nm) required for PL makes achieving the target performance more challenging, as the design space is more restricted. In contrast, the

EBL-based generator model provides access to finer geometric degrees of freedom, enabling the optimizer to more accurately shape wavelength-dependent modal interference patterns and thereby achieve improved spectral performance. Consequently, the EBL model demonstrates enhanced transmission characteristics, reaching approximately 94% efficiency compared to roughly 80% observed in the PL design. This higher transmission translates directly to a lower insertion loss of 0.25 dB for EBL, whereas the PL model is limited to 0.3 dB. Ultimately, while PL offers better scalability for manufacturing, the larger latent space and higher resolution of the EBL-based generator allow the optimizer to find a more efficient solution.

C. Broadband Photonic Mode Converter

A broadband mode converter was designed using the PL-based generator model, aiming to transform the fundamental TE_0 mode at the input into the first-order TE_1 mode at the output. The device occupies a compact footprint of only $2.75 \times 2.75 \mu\text{m}^2$. During the optimization process, the target function was defined to maximize the modal overlap with the TE_1 electric field profile at the output port.

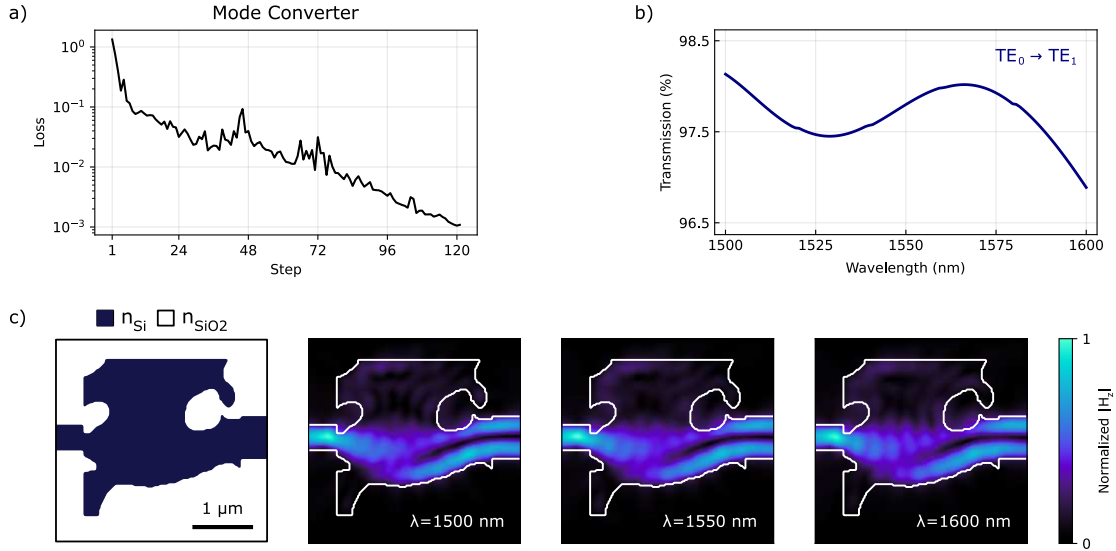


FIG. S7. Broadband photonic mode converter performance. (a) Evolution of the optimization loss over 120 iterations, decreasing from an initial 1.74 to a minimum of 9.5×10^{-3} . (b) Simulated transmission spectra showing a consistently high TE_0 -to- TE_1 conversion ratio of 96–98% across 1500–1600 nm, reaching ~99% efficiency at 1550 nm, corresponding to an insertion loss of only 0.03 dB. (c) Optimized permittivity profile of the device (left) alongside normalized magnetic field distributions ($|H_z|$) at wavelengths of 1500, 1550, and 1600 nm, highlighting successful broadband TE_1 mode conversion.

As illustrated in Fig. S7(a), the optimization converged after approximately 120 iterations, with the loss decreasing from an initial value of 1.74 to a minimum of 9.5×10^{-3} . The transmission into the TE_1 mode remained consistently high throughout the optimization, fluctuating between 96% and 98% (Fig. S7(b)). The final transmission efficiency of ~99% corresponds to an insertion loss as low as 0.03 dB. The optimized device geometry is depicted in Fig. S7(c). The input waveguide width is 450 nm, gradually expanding to 700 nm at the output. Field distributions simulated at 1.50, 1.55, and 1,600 nm confirm the broadband behavior of the device. The normalized FDFD field maps clearly demonstrate the successful conversion into the TE_1 mode, characterized by the emergence of two symmetric intensity

lobes at the output waveguide.

The observed performance disparity, where the EBL generator model converges to a loss of 3×10^{-4} while the PL generator model reaches 9.5×10^{-3} , is again a direct consequence of the trade-off between fabrication constraints and design freedom. Specifically, as the minimum feature size increases from 60 nm to 150 nm, the PL generative model is forced to generate larger-scale features, which inherently lack the fine-grained control to manipulate ultrabroadband light. Consequently, while the EBL generator-based designs achieve near-ideal performance within $2.1 \times 2.1 \mu\text{m}^2$ footprint, the PL generator-based design requires an expanded $2.75 \times 2.75 \mu\text{m}^2$ area to redistribute the modal power and compensate for the reduced efficiency of larger dielectric features. Furthermore, the optimization for the PL generator-based device design is conducted in a lower-dimensional 8×8 latent space vector, compared to the 10×10 latent space vector used for the EBL generator-based design, which imposes a more rigid constraint on the available parameter space. This reduction in tunable degrees of freedom necessitates a more exhaustive search for an optimal solution, explaining the increased iteration count required to navigate the high-dimensional cost landscape under stricter geometric priors. Despite these fabrication limitations, both devices exhibit exceptional performance: the PL generator model achieves a transmission efficiency of approximately 99% (0.03 dB insertion loss), while the EBL-based model achieves a transmission efficiency of approximately 98% (0.07 dB insertion loss). These results confirm that our generative approach can successfully achieve complex modal transformations using fabrication-compatible geometries across different lithographic regimes.

REFERENCES

- [1] Hammond, A. M., Oskooi, A., Johnson, S. G. & Ralph, S. E. Photonic topology optimization with semiconductor-foundry design-rule constraints. *Optics Express* **29**, 23916–23938 (2021). URL <https://opg.optica.org/oe/abstract.cfm?URI=oe-29-15-23916>.
- [2] Qian, X. & Sigmund, O. Topological design of electromechanical actuators with robustness toward over- and under-etching. *Computer Methods in Applied Mechanics and Engineering* **253**, 237–251 (2013). URL <https://www.sciencedirect.com/science/article/pii/S0045782512002721>.
- [3] Zhou, M., Lazarov, B. S., Wang, F. & Sigmund, O. Minimum length scale in topology optimization by geometric constraints. *Computer Methods in Applied Mechanics and Engineering* **293**, 266–282 (2015). URL <https://www.sciencedirect.com/science/article/pii/S0045782515001693>.
- [4] Christiansen, R. E., Michon, J., Benzaouia, M., Sigmund, O. & Johnson, S. G. Inverse design of nanoparticles for enhanced raman scattering. *Optics Express* **28**, 4444–4462 (2020). URL <https://opg.optica.org/oe/abstract.cfm?URI=oe-28-4-4444>.
- [5] Caseman, R. noise (version 1.2.2) [python package]. <https://github.com/caseman/noise> (2015). Accessed: 2026-01-29.